Understanding Gas-Phase Ammonia (NH$_3$) Chemistry in Proto-Planetary Disks

Lauren Chambers

Advised by Hector Arce[1], Karin Öberg[2], and Ilse Cleeves[2]

[1]Yale University, [2]Harvard-Smithsonian Center for Astrophysics

A thesis presented in partial fulfillment of the
requirements for the degree of Bachelor of Science

Department of Astronomy
Yale University

May 4, 2017

Abstract

Protoplanetary disks are the dense and radiated regions of gas and dust around young stars that ultimately form planetary systems. Ammonia (NH_3), one of the primary molecular carriers of nitrogen and an important chemical ingredient in Earth-based life, is both present in the interstellar medium and created by chemical processing within protoplanetary disks. NH_3 has been observed in one such protoplanetary disk system; Salinas et al. (2016) observed an ammonia abundance relative to water of 33–84% in surface-emitting regions of the TW Hydra disk, a high ratio compared to the 0.3–2% ice-phase ammonia-to-water ratio observed in comets. This discrepancy could be explained by differences in ice-phase versus gas-phase chemistries, or by spatial variation of NH_3 chemistry within disk regions subject to different physical and chemical environments. Using a closed-box numerical chemical model with user-defined physical parameters, we model the production and destruction of NH_3 in protoplanetary disks at six locations sampling a range of physical and chemical conditions. We examine the dependency of disk ammonia chemistry upon inherited interstellar ammonia, grain-surface ammonia formation processes, and ionizing radiation in the form of cosmic rays, X-rays, and ultraviolet radiation. We ultimately find that (1) a high gas-phase NH_3/H_2O ratio at the disk surface can exist simultaneously with a low ice-phase NH_3/H_2O in the disk midplane; (2) regional differences in ammonia chemistry occur due to varying rates of ionization in the disk, with a strong dependence on cosmic rays; and (3) in the case of a modulate cosmic ray flux, it becomes necessary to include inherited ammonia to reach observed cometary abundances of ammonia ice in the disk.

Contents

Chapter 1:
Introduction

1.1 Proto-planetary Disks

Protoplanetary disks are dynamic regions of gas and dust around young stars that evolve over millions of years to ultimately form planets. Protoplanetary disks are the result of the gravitational collapse of a stellar birth cloud combined with the conservation of angular momentum (Shu et al., 1987). The typical disk extends out to ~20–230 AU (Andrews et al., 2010; Isella et al., 2009). While they are generally flat close to the star, they are often flared at outer radii (e.g., Smith et al., 2005). Disk structures and evolutionary scenarios depend on the dynamic influ-

Figure 1.1: One of the highest-resolution images of a proto-planetary disk: pictured, the face-on TW Hydra disk as imaged by ALMA in 2016. Note the complex radial structures, both at larger scales and at smaller scales (as emphasized by the inset image, which represents a scale of 1 AU). Image credit: S. Andrews (Harvard-Smithsonian CfA), ALMA (ESO/NAOJ/NRAO) (reproduced with permission from the author).

ences of ionizing radiation, magnetic fields, chemical composition, turbulence, and gravity, among other factors. As such, the chemical and physical properties of planets forming within the disk depend on the specific time and place of their formation. Thus, the astrophysical (and astrochemical) quest to understand planets is informed by an understanding of the properties and processes inherent to these protoplanetary disks (Cleeves, 2015; Williams & Cieza, 2011).

Figure 1.2: Visualization of the stages and processes of star formation. From least to most evolved, clockwise from the upper left: giant molecular clouds, protostars, proto-planetary disks, and planetary systems. Image from Cleeves (2015).

1.1.1 Disk Formation and Classification

Protoplanetary disks are a phase in the greater arc of star formation, which is illustrated in Figure 1.2. Stars originate in giant molecular clouds, or 10^4–10^6 $M_\odot$ gravitationally-bound clouds of cold gas and dust that span tens of parsecs across. They are composed of molecular gas, primarily in the form of H_2, which is not dissociated or ionized due to both the 10-20 K temperature of the cloud and the efficient shielding from surrounding radiation fields. Within these clouds form over-dense filamentary structures which are nurseries for the smaller, localized 'cores', on the order of ~ 0.1 pc. These cores collapse into stars when their internal force of gravity overcomes the internal pressure due to temperature, turbulence, and magnetic fields (Dame et al., 2001; Hartmann, 1998).

As a molecular core collapses under its own gravity, any rotation of the original cloud is amplified due to conservation of angular momentum. Thus, gravitational collapse leads to the creation of an rotating disk, in which material becomes confined to a plane of rotation. In addition to rotating, the disk is accreting; as gas and dust in the disk interact via collisions, some material loses energy and falls (accretes) onto the pre-main sequence star, which is not yet fusing hydrogen into helium at its core. Some material also gains energy from collisions, leading to the expulsion of high-energy material out of the disk system. Over time, the accretion of in-falling material and the expulsion of high-velocity material leads to the diffusion of the stellar envelope, leaving a compact, settled disk (see Figures 1.2 and
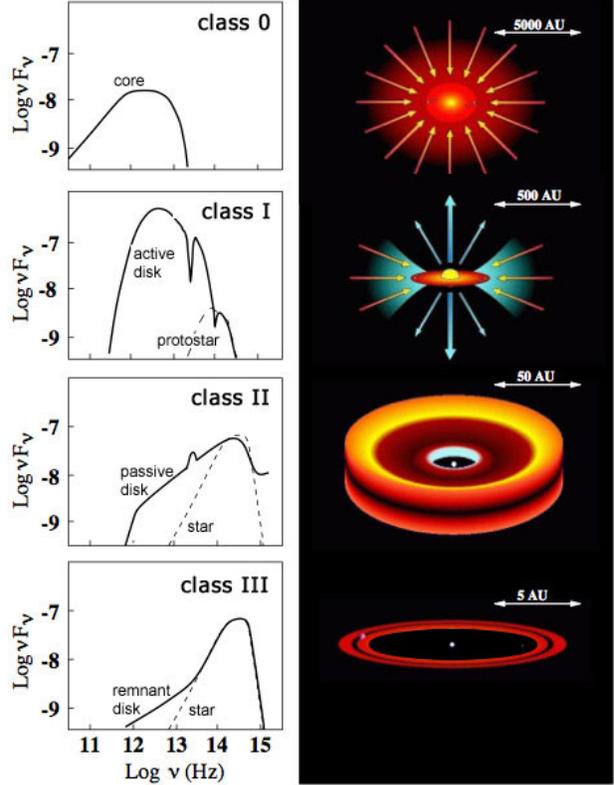
Figure 1.3: Rough visualization of the classes and characteristics of young stellar objects, increasing in maturity from 0 to III. Note that more mature classes correspond to hotter blackbody curves that peak at higher frequencies, as the protostar warms and evolves into a main sequence star. Additionally, note that the lower-frequency spectral feature from the dusty disk becomes less dominant as the object accretes, matures, and becomes less diffuse. Image from Isella (2006) (reproduced with permission from the author).

1.3). The stellar core is simultaneously growing and heating as it transitions from a protostar (a non-Hydrogen-fusing hot, dense object in a diffuse dusty envelope) to a deuterium-burning protostar (Stahler, 1988) and ultimately to a main-sequence (Hydrogen-fusing) star. Astronomers have defined three different kinds of young protostars by mass: Herbig Ae ($1M_\odot < M_* < 8M_\odot$), T Tauri ($0.08M_\odot < M_* \leq 1M_\odot$), and young brown dwarfs ($M_* < 0.08M_\odot$) (Williams & Cieza, 2011; Hartmann, 1998).

Young stellar objects, and the disks that surround them, are classified according to the shape of their observed infrared spectrum. These classifications also correlate with

stages of disk evolution, from an embedded protostar to a protoplanetary disk. These stages were first defined by Lada (1987) as three classes of young stellar objects – I, II, and II – delineated by the slope of the objects' spectral energy distribution (SED). An earlier class, class 0, was later added by Andre et al. (1993). The SED indicates the dust emission from reprocessed radiation from the growing protostar; the youngest protostars (Class 0) are dominated by long-wavelength emission from the dusty envelope, while mature systems are T-Tauri stars with stellar blackbody spectra almost free of dust (Class III). Thus, as YSOs evolve, their spectrum spans a smaller wavelength range, and the slope of the spectrum in optical wavelengths becomes increasingly negative. The four classes, 0, I, II, and III are thus parametrized by the slope of the continuum emission spectrum, α_{IR}:

$$\alpha_{IR} = \frac{d \log \nu F_\nu}{d \log \nu} \tag{1.1}$$

The four classes are illustrated in Figure 1.3, and are listed with their corresponding SED slopes and evolutionary stages in Table 1.1.

As illustrated in Figure 1.3, disk-like structure is already present in Class 0 YSOs (i.e. protostars). In Class II objects (i.e. T-Tauri stars), accretion onto the central protostar slows to the extent that disk material will mostly remain in the disk and ultimately form into planets, rather than falling onto the core. Thus, disks around Class II protostars are considered protoplanetary rather than protostellar. While Class 0 and I stages span ~ 0.5 Myr, Class II protostars' disk lifetimes span 1–10 Myrs. Class II stars are more easily observable in optical wavelengths than their earlier counterparts, as the envelope has diffused and the remaining dust becomes is confined to the flat midplane. (Williams & Cieza, 2011; Hartmann, 1998).

Finally, Class III objects have lost almost all of their gas-rich disks, and thus Class III star/disk systems have SEDs very similar to a sole stellar blackbody (bottom-most plot in Fig. 1.3). This object class represents a continuum ranging from transition disks, which

have weak near-IR emission yet still maintain strong mid- and far-IR emission, to debris disks that are composed primarily of large dust grains and planetesimals and thus are very IR-weak (Hartmann, 1998).

Table 1.1: Classification of young stellar objects (from Williams & Cieza (2011))

Class	SED slope	Physical properties	Observational characteristics
0	-	$M_{env} > M_{star} > M_{disk}$	No optical or near-IR emission
I	$\alpha_{IR} > 0.3$	$M_{star} > M_{env}$ M_{disk}	Optically obscured
Flat-spectrum	$-0.3 < \alpha_{IR} < 0.3$		Intermediate between Class I and II
II	$-1.6 < \alpha_{IR} < -0.3$	M_{disk}/M_{star} 1%, M_{env} 0	Accreting disk; strong Hα and UV
III	$\alpha_{IR} < -1.6$	$M_{disk}/M_{star} \ll 1\%$, M_{env} 0	Passive disk; no or very weak accretion

1.1.2   Disk Physical Structure & Processes

Knowledge of the structure and characteristics of protoplanetary disks are the results of decades of observations. For instance, disk size and structure has been observed at optical wavelengths with Hubble through 'proplyds', or shadows of disks cast upon background nebulae (McCaughrean & O'dell, 1996). The rotation of disks has been observed using interferometry to detect bipolarity in radial velocities at millimeter wavelengths (Sargent & Beckwith, 1987). The dust in disks has been observed, mapped, and characterized in mm, sub-mm, and infrared wavelengths (e.g., Andrews & Williams, 2005; Megeath et al., 2012; Draine, 2006). At the same time, the radiative field experienced by disks has been predicted using radiative transfer, and the density distribution and spatial evolution of disks have been calculated using hydrodynamical theory. Thus, thanks to both theorists and observers, our astrophysical understanding of the properties of protoplanetary disks is growing (Williams & Cieza, 2011).

Density Distribution

The distribution of gas and dust in a protoplanetary disk can be modeled roughly by balancing the competing forces present: gravity, pressure, and along the radial direction, a centrifugal force. The density distribution of an axisymmetric rotating disk in hydrostatic equilibrium can be analytically determined by solving the momentum equation for a constant velocity. In cylindrical coordinates (r, ϕ, z), the radial r-component balances the radial force of gravity, the centrifugal force of rotation, and the pressure within the disk (from Durisen (2011), eq. 10):

$$\frac{dv_r}{dt} + \vec{v} \cdot \nabla v_r = 0 = -\frac{1}{\rho}\frac{dP}{dr} + r\Omega^2 - \frac{GM_*}{r^2} - \frac{d\Phi_{disk}}{dr} \tag{1.2}$$

where v is the (constant) velocity of the disk, ρ is the density, P is the pressure, Ω is the angular velocity, G is the gravitational constant, M_* is the mass of the central star, and Φ_{disk} is the gravitational potential due to the mass of the disk. Similarly, the vertical z-component balances the vertical force of gravity and pressure (from Durisen (2011), eq. 11):

$$-\frac{1}{\rho}\frac{dP}{dz} - \frac{GM_*z}{r^3} - \frac{d\Phi_{disk}}{dz} = 0. \tag{1.3}$$

Though I will omit the lengthy derivation, Lynden-Bell & Pringle (1974) determined that the surface density (i.e. radial profile assuming azimuthal symmetry) of the disk is best modeled by an exponentially-tapered power law (from Williams & Cieza (2011), eq. 4):

$$\Sigma(R) \propto \exp\left[-\left(\frac{R}{R_c}\right)^{2-\gamma}\right] \tag{1.4}$$

where R_c is the characteristic radius and γ is the exponential change of the disk viscosity ν with radius ($\nu \propto R^\gamma$). From the combination of vertical and radial models, the density for an azimuthally symmetric disk in hydrostatic equilibrium is (as written in Williams & Cieza

(2011), eq. 5):

$$\rho(R, Z) = \frac{\Sigma(R)}{\sqrt{2\pi}H} \exp\left[-\frac{1}{2}\left(\frac{Z}{H}\right)^2 \right] \tag{1.5}$$

where $\Sigma(R)$ is as above and $H(R)$ is the scale height (Williams & Cieza, 2011; Durisen, 2011).

Composition: Gas & Dust

Protoplanetary disks are made of gas and dust. Dust grains are composed of primarily silicates, though graphite and polycyclic aromatic hydrocarbons (PAHs) are also common (Draine, 2003). Dust grains are influential on the chemistry of disks for the surface area they provide for molecules to freeze, meet, react, and develop into more complex molecules. Molecular ices grow in layers on these grain surfaces. Thus grain surface chemistry is especially important in low-temperature areas where atoms and molecules have long residence times on grains (due to reduced rates of thermal and photodesorption). Since ice-phase chemistry occurs on the surface of dust grains, the terms 'ice-phase' and 'grain-phase' are used interchangeably throughout this paper, and the notation X(gr) will be used to denote the grain phase of any molecule X. While interstellar dust ranges in size from ~ 5 nm to 1 μm, dust grains in disks coagulate and grow over time, vary in size from fractions of a micron to tens of cm to planetesimals (Draine, 2006). Even with grain growth, however, the smaller grains constitute the vast majority of the total dust surface area, and thus dominate chemical effects. Gas in disks, like gas in the interstellar medium, is dominated by molecular hydrogen (H_2). As astrochemists gain a deeper understanding of the effects of disk environment on disk gas and dust chemistry, observations of gas- and grain-phase chemistry ca go beyond chemistry to indicate the physical structure and characteristics of the disk (Cleeves, 2015).

Radiation

The temperature and chemistry of the gas and dust inside a protoplanetary disk is determined in large part by the interaction of incident radiation with disk material. All disks are exposed

to ultraviolet radiation and X-ray radiation from both the central star and nearby sources, as well as galactic cosmic rays. Due to scattering and attenuation within the disk, temperatures can vary from just a few Kelvin within the most shielded regions to hundreds of Kelvin at the most radiated regions. In addition to heating, ionization makes chemical interactions possible in cold regions by creating gas-phase ions that combine with both gaseous neutral molecules and frozen molecules on dust grains. With respect to radiation, disks are generally divided into three regions: the hot photon-dominated region, the warm molecular layer, and the frozen midplane (Bergin, 2009).

The photon-dominated region exists on the disk surface, where radiation from both the central star and the surrounding environment are strongest. Here, due constant bombardment by dissociating photons, complex molecules have short lifetimes and the gas is dominated by simple ions. Furthermore, the higher temperatures and stronger radiation prevent molecules from sticking (freezing) onto dust grains, and so there are very low abundances of ice-phase molecules. The warm molecular layer exists below the photon-dominated region, where the radiation is weaker and more complex molecules can begin to form. Finally, the midplane is coldest and innermost region of the disk, around the plane of rotation ($Z = 0$), where the gas and dust are shielded from all but the highest-energy photons (Aikawa et al., 2002). Here, complex molecules are abundant and gas-phase molecules easily freeze out, accumulating onto grains and forming ices many monolayers thick (Tielens & Hagen, 1982).

Evolution

With time, the disk undergoes changes in structure and composition as a result of various forms of particle interactions, including dust grain growth and settling, photoevaporation, and viscous transport (to be explained in section E) .

Over the disk lifetime, dust grains will collide, stick to one another, and ultimately grow into larger dust grains. Grain growth is important not just because it is the first stage of planet formation, but because it also facilitates radial drift, which changes the dust density

distribution of the disk. When grains are small, they travel around the disk along side the gas surrounding them, in slightly non-Keplerian motions due to the force of pressure acting on the gas. However, as grains grow, their motions become Keplerian and separate from the gas motion, leading to increased friction and drag on the dust due to the velocity difference. This in turn causes the dust grains to fall inward to an orbit at smaller radius (radial drift) and to fall downward towards the $Z = 0$ plane of rotation (dust settling). The twin processes of radial drift and dust settling lead to larger dust grains being more heavily concentrated at smaller radii and smaller disk heights (Williams & Cieza, 2011). Grain growth and dust settling are shown from stages (a) to (b) in Figure 1.4.

Light-matter interactions also have a role to play in disk evolution. Interactions of disk material with high-energy incoming far-UV and X-ray photons from its central star result in disk evaporation. At first, this photoevaporation occurs at the most central disk regions (at small R), where photoevaporated material is quickly replaced by accreting matter, allowing outer regions to be shielded. However, in more mature disks with slowed accretion rates, the central infalling mass is not immediately replaced by infalling mass coming from greater radii. This leaves a hole at the center of the disk, and allows photoevaporation to occur in a runaway feedback loop at small radii and quickly diffuse all of the disk's gas (Williams & Cieza, 2011). This process is illustrated in part (c) of Figure 1.4 .

Once a protoplanetary disk is formed, planet formation can begin. However, much work remains to be done to explain this final stage. While some observations of giant planet formation have been obtained, the theoretical 'how' and 'when' are still uncertain. Additionally, there is a gap in the theory, called the meter-sized barrier, describing how dust grains gradually grow into planets and planetesimals without being destroyed and re-fragmented in collisions (Weidenschilling, 1977).
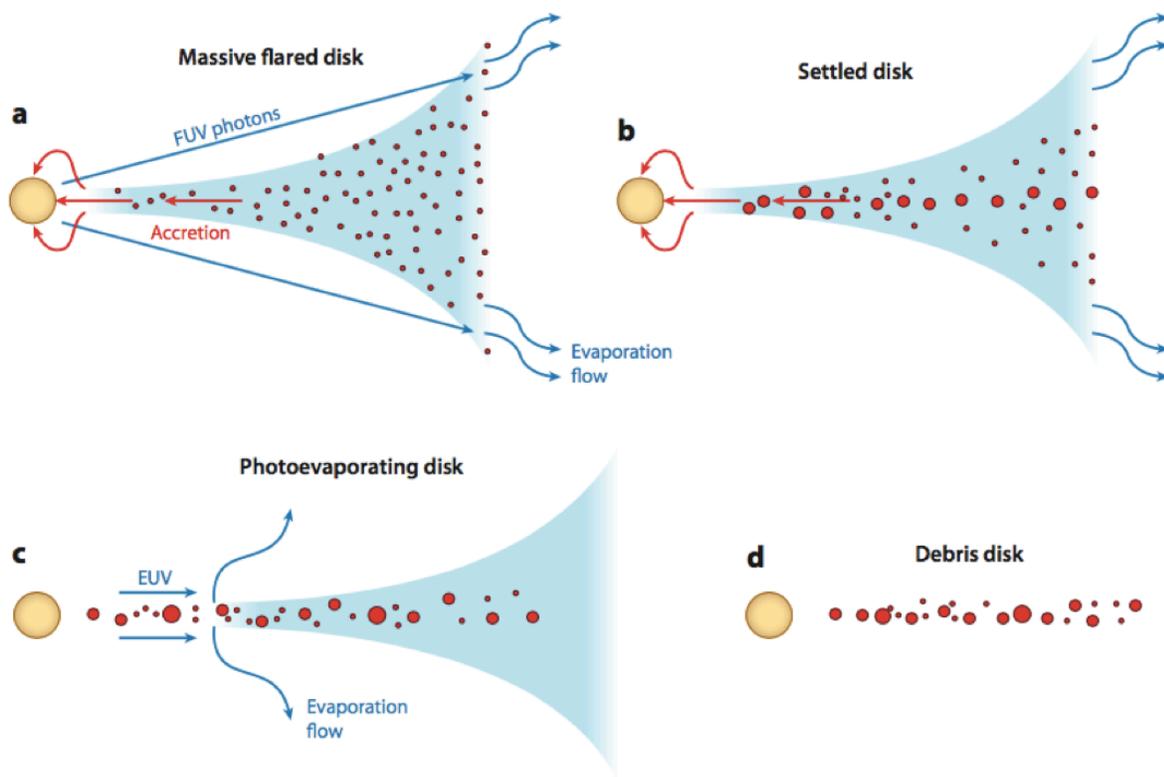
Figure 1.4: Stages of disk evolution, in which disk gas is shown as blue, dust shown as red circles, accretive processes as red arrows, and evaporative processes as blue arrows. In stages (a) and (b), the disk is dominated by accretion, dust grains settle and grow, and the only surface of the disk is photoevaporated. In stage (c), the accretion rate has slowed such that accretion does not replace the void left by accreted material quickly enough, and runaway photoevaporation can occur. By stage (d), the protoplanetary disk has become a gas-less debris disk. Image from Williams & Cieza (2011), Figure 6 (reproduced with permission from the author).

1.1.3   Observations

Observations of disks were first limited to their spectral energy distributions (SEDs), or infrared observations with very low spatial and spectral resolution. Astronomers studied disk SEDs to determine how gas and dust absorbed and scattered starlight in an unresolved disk system (Lada & Wilking, 1984). With the 1990 launch of *Hubble* and its unparalleled imaging capabilities, astronomers discovered "proplyds:" visible and highly resolved shadows of circumstellar disks cast upon bright gaseous background nebulae. These strikingly detailed images provided insight into disk morphology, density, and mass (McCaughrean & O'dell, 1996).

In recent years, the study of protoplanetary disks has further advanced with the advent of infrared space observatories such as the Infrared Astronomy Satellite and the Spitzer Space Telescope Hubble Space Telescope, and now interferometers such as the Atacama Large Millimeter Array (ALMA). Today, ALMA observations allow astrophysicists to resolve features down to 1 AU, with greater spectral and spatial resolution than ever before (Andrews et al., 2016).

However, many limitations remain. Even the best observatories still do not have the necessary resolution to see into the terrestrial planet forming zone within the inner ~1 AU. Furthermore, as with all astronomical observations, results are difficult to interpret due to the projection of three-dimensional disks onto the two-dimensional plane of the sky; as a result, certain aspects of disk structure (such as vertical or radial distributions) must be extrapolated with imperfect radiative transfer models, rather than directly observed.

1.2 Chemical Modeling of Disks

Since the early 1990s, chemical models of disks have been calculated by solving time-dependent reaction equations over the lifetime of the disk. Once astrochemists moved on from inaccurate assumptions of thermochemical equilibrium, the field quickly grew to explore diverse aspects of disk chemistry.

Early efforts often focused on characterizing chemistry in different regions within the disk. Aikawa et al. (1996) investigated the dependence of chemical evolution on the physical disk environment. Examining the behavior of CO, specifically, they found depletion of gas-phase CO in the outer disk at radii beyond the critical radius R_{crit}, where the thermal desorption rate of CO equals the adsorption rate. The freezing of CO onto grains beyond R_{crit} thus led to depletion of gas-phase CO by a few orders of magnitude within 10^5-10^6 years. Today, R_{crit} is referred to as a "snowline," and is used to delineate between gas-dominated and ice-dominated regions. Aikawa & Herbst (1999) was one of the first studies

to model the chemical evolution of disks in two dimensions, both radial and vertical. They compared resulting column densities with observations, exploring the chemical dependencies of different molecules on UV radiation, dust settling, and gas and dust densities. Later, Aikawa et al. (2002) was one of the first astrochemical modeling studies to adopt a vertical temperature gradient, using the physical disk model first conceptualized by D'Alessio et al. (1999). They found that gaseous abundances peaked in a warm intermediate layer above the midplane yet below the disk surface, where thermal desorption occurs and UV radiation is shielded by upper layers.

Subsequent astrochemical studies improved theoretical understandings of the external and internal factors and processes that affect disk chemistry. Bergin et al. (2003) characterized the stellar far-UV radiation present in disks, ultimately determining that the FUV field is dominated not by continuum emission but rather by Lyman α line emission. The importance of Lyα radiation was previously unexplored within astrochemistry, and Bergin et al. (2003) alerted the field to the importance of interactions of Lyα with specific molecules, namely H_2O, CN, and HCN. Fogel et al. (2011) later determined how both Lyα radiation and vertical dust settling influenced chemical evolution in disks. They found that disks with greater settling have smaller freeze-out regions, and thus larger intermediate warm molecular layers, leading to increased column densities for many molecules.

In recent years, astrochemical observations and models have become sufficiently sophisticated as to provide insights into, and even constrain, disk physics. Cleeves et al. (2013a) examined for the first time how a decreased flux of cosmic rays in disks, due to interactions with stellar winds and/or magnetic fields, might affect ionization and chemical evolution in disks. They find that CR modulation can lead to an 1–3 order of magnitude reduction in the ionization rate. If this modulation is present, then short-lived radionuclides, rather than cosmic rays, would be the primary source of ionization in shielded regions of the disk (Cleeves et al., 2013b). Finally, Cleeves et al. (2015) used astrochemistry as a probe to constrain the cosmic ray rate in TW Hydra. By comparing 12 line observations of TW Hydra to results

from various models of cosmic ray exclusion, they constrain the CR ionization rate in disks to be $\lesssim 10^{-19}$ s^{-1} – more than two orders of magnitude below the interstellar cosmic ray rate.

1.3 Interstellar Ammonia

Ammonia is one of the primary molecular bearers of nitrogen, and one of the most common polyatomic molecules found in interstellar space. Indeed, nitrogen is an integral component to life on Earth, and some studies suggest direct connections between interstellar ammonia and the formation of biologically important molecules in space. For instance, lab studies conducted by Bernstein et al. (2002) suggested that the UV processing of ammonia ice and other simple interstellar ice molecules can lead to the formation of amino acids. As amino acids were previously thought to be produced only in liquid water on planetary surfaces, an interstellar photochemical origin for amino acids could greatly broaden the conditions necessary for the development of life. Thus, it is clear that the study of ammonia is important to both astrochemistry and astrobiology.

The nitrogen available for the production of ammonia in disks has been shown to come from the inherited interstellar environment. While there is some uncertainty regarding the original molecular form of nitrogen in protoplanetary disks, chemical/physical models of nitrogen-bearing molecules by Schwarz & Bergin (2014) suggest that the nitrogen is inherited by disks primarily in the form of atomic and molecular nitrogen (N and N_2, respectively). Models with direct inheritance of nitrogen in the form of NH_3 or $NH_3(gr)$ showed the bulk nitrogen becoming trapped on grains. Schwarz & Bergin (2014) further suggests that nitrogen is predominantly inherited from the interstellar medium in a volatile, rather than frozen, form. Indeed, this prediction is supported by data from observations of molecular cloud cores, protostars, and the *Spitzer* c2D Legacy ice survey, which Öberg et al. (2011) used to determine that only ~10–35% of nitrogen inherited by protoplanetary disks is in the form of protostellar ices (NH_3 and XCN). However, this result also suggests that some ammonia

might be directly inherited from the interstellar medium; most of this ~10–35% of nitrogen inherited as ice is in the form of $NH_3(gr)$.

Astrochemists have used numerical modeling, cryogenic lab experimentation, and direct observations to characterize the formation and distribution of interstellar ammonia ice. Tielens & Hagen (1982) first used numerical modeling to predict that ammonia would be present in interstellar ices on grains. Two decades later, Charnley et al. (2001) modeled various formation processes of ammonia ice, and determined that the freeze-out of gas-phase ammonia alone would lead to a depleted interstellar $NH_3(gr)/H_2O(gr)$ ratio; the formation of $NH_3(gr)$ by the hydrogenation of N(gr) on grains (N(gr) + H(gr) -> NH(gr), and so on) was necessary to achieve the observed $NH_3(gr)/H_2O(gr)$ ratio of ~10%. Another decade later, Faure et al. (2013) derived the specific branching ratios for the formation and destruction of ammonia, using it to predict NH_3 ortho-to-para ratios in the cold ISM. Le Gal et al. (2014) represent how far chemical modeling has come; they present sophisticated chemical modeling of gas-phase processes for nitrogen hydrides in dark interstellar clouds, incorporating ortho-to-para conversion and nuclear spin branching ratios into their chemical reaction network. Additionally, they describe in detail the interactions and dependency of nitrogen hydride abundances on the initial abundance of sulfur and the initial ratio of carbon to oxygen. These models demonstrate the complexities and particularities inherent to the creation of even a simple molecule like ammonia in interstellar space.

Hiraoka et al. (1995) first used cryogenic laboratory chemical experiments to demonstrate the formation of NH_3 by the interaction of frozen N(gr) with free H atoms at 10–30K. Two decades later, Fedoseev et al. (2015) reexamined formation of ammonia ice in conditions more faithful to the ISM, in mixtures of H_2O and CO ice. They characterized the formation of $NH_3(gr)$ on dust grains, specifically focusing on the intermediate role of HNCO(gr) in the presence of CO(gr). This work supported the numerical results of Charnley et al. (2001), identifying the hydrogenation of N on grains as an efficient pathway for ammonia formation, and furthermore suggesting the early co-formation of ammonia with water due to the speed

with which this hydrogenation occurred.

In the past decade, observational methods have improved enough to enable direct detection of interstellar ammonia ice. Bottinelli et al. (2010) used *Spitzer* data to characterize interstellar ammonia ice for the first time in low-mass young stellar objects, suggesting an ice-phase $NH_3(gr)/H_2O(gr)$ ratio of 5.5%±2.0% in low-mass protostars, with ~10–20% of all available nitrogen frozen into nitrogen-bearing ices. In a sweeping study of interstellar ices, Öberg et al. (2011) built upon previous work and included data from 10 new protostars observed with *Spitzer*, determining the ice-phase ammonia-to-water ratio to be consistently ~ 5% in low- and high-mass protostars. The small variance in the $NH_3(gr)/H_2O(gr)$ ratio across many protostar observations (ranging only from 2.1% to 5.7%) supports that ammonia ice is produced early in the disk lifetime, co-forming with water, and is not sensitive to stellar environment.

Though ammonia ice has never been directly observed in a protoplanetary disk, it has been studied in Solar System comets. The chemistry of cometary nuclei today is though to be consistent with their chemistry at the time of comet formation in the icy midplane of our Solar System's protoplanetary disk. Thus, studies of cometary chemistry are often used as proxies for studies of disk ice. Mumma & Charnley (2011) found that ammonia is present in comets with an abundance relative to water of ~ 0.3–2%. When compared with the work of Öberg et al. (2011), this suggests a depletion of ammonia during the maturation of the disk from a diffuse protostar to a mature comet-forming disk.

Long before ammonia ice was detected, ammonia gas became the very first polyatomic species detected in interstellar space when Cheung et al. (1968) used the 20 ft. mm antenna at the Hat Creek Station of University of California's Radio Astronomy Laboratory to detect a radio signal in the interstellar medium, near the galactic center. However, detections of ammonia gas in protoplanetary disks have been elusive. Before 2016, previous work had only established upper limits in disks of <20% NH_3/H_2O (Mandell et al., 2012). Finally, Salinas et al. (2016) published the first *Herschel* detection of ammonia gas in a protoplanetary disk,

inferring an NH_3/H_2O ratio of 33–84% in TW Hydra.

1.4   TW Hydra and Ammonia

TW Hydra is a pre-main sequence T-Tauri star, about 10 Myr old, with a mass of ~0.8 $M_\odot$ and located 54 ± 6 pc from the Sun. TW Hydra is notable for its gaseous circumstellar disk that is oriented face-on within the plane of the sky and perpendicular to the line of sight, thus allowing for radially resolved observations in the optical and infrared regimes (Andrews et al., 2012). Due to its proximity and orientation, TW Hydra is one of the most well-observed protoplanetary disk systems.

With the advent of *Herschel*, TW Hydra became the subject of many high spectral resolution observations. As a result, it was the first disk in which deuterated hydrogen (HD) was observed, constraining the disk's total gas mass (Bergin et al., 2013). TW Hydra is also the only protoplanetary disk in which gas-phase ammonia (NH_3) has been directly observed (Salinas et al., 2016). The NH_3 1_0–0_0 line (572.49817 GHz) was observed as part of a 5.43 hour observation using *Herschel* on June 15, 2010 (see Fig. 1.5).

Figure 1.5: *Herschel* observations of the NH_3 1_0–0_0 and the H_2O 1_{10}–1_{01} lines in TW Hydra. Image from Salinas et al. (2016), Figure 1a (reproduced with permission from the author).

Radiative transfer was used in combination with four distributional models, 'Ep' , 'Em', 'Cp', and 'Cm', shown in Figure 1.6. The distributional models incorporate two possibilities for radial ammonia distribution: either compact gas distribution emitting out to 60 AU ('C'), or extended gas distribution emitting out to 196 AU ('E'). The models also incorporate two possibilities for vertical ammonia distribution: either ammonia is co-spatial with water

and thus most highly concentrated in the intermediate to upper disk photodesorption layers ('p'), or ammonia and water are distributed like H_2 and are thus most heavily concentrated around the midplane ('m'). The four models together corresponded to an ammonia vapor mass ranging from 7.0×10^{20}–1.1×10^{22} g and an ammonia-to-water gas ratio of $7\%^{+9\%}_{-5\%}$ – $84\%^{+61\%}_{-36\%}$.

From the Salinas et al. (2016) result, the measured gas-phase ammonia-to water ratios that best agree with previous observations of cometary NH_3/H_2O ratios correspond to the compact midplane ('Cm') and extended midplane ('Em') distributional models: 7–15% and 19–38% NH_3/H_2O respectively. However, these two models assume ammonia and water concentration in the frozen midplane, regions that would not undergo sufficient non-thermal desorption to explain the resulting observed ammonia abundances. Salinas et al. (2016) suggest
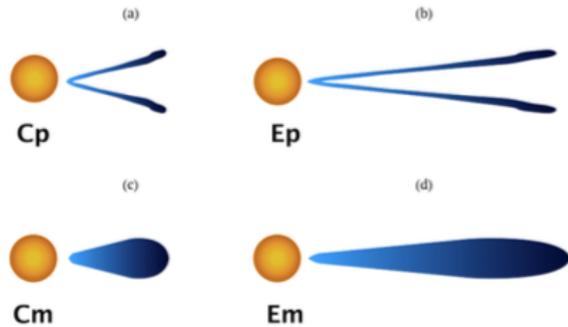
Figure 1.6: The four proposed distributions of water (and thus of ammonia) adopted and evaluated by Salinas et al. (2016). The models labeled 'C' confine emission to the inner 60 AU, while the models labeled 'E' extend emission out to 196 AU. The models labeled 'p' restrict emission to a thin photodesorption layer at the disk surface, while the models labeled 'm' assume both NH_3 and H_2O to exist at a constant ratio with the bulk H_2 gas. Image from Salinas et al. (2016), Figure 3 (reproduced with permission from the author).

that such vapor might be freed during collisions of icy bodies, on the order of ~10^3–10^6 comets destroyed in the disk per year – an explanation that they admit is unlikely. In this work, we choose to focus on the more likely scenarios and will compare our results to the surface-emitting compact photodesorption layer ('Cp') and extended photodesorption layer ('Ep') models. Together, these two models correspond to an ammonia vapor mass ranging from 7.0×10^{20}–12.0×10^{20} g and an ammonia-to-water gas ratio of $33\%^{+11\%}_{-11\%}$ – $84\%^{+61\%}_{-36\%}$.

This range of ratios, though admittedly large, is significantly larger than estimates of the ammonia-to-water ice ratio in disks, ~0.3–2% (Mumma & Charnley, 2011). The ice-phase ratio was obtained from observations of over 10 Solar System comets which formed in the

cold midplane of our own Solar System's young disk and thus which are thought to have maintained the ice chemistry of the disk. The discrepancy between the 0.3–2% ice ratio and the 33-84% gas ratio suggests a gap in astrochemical understanding, potentially due to unexpected chemical processes, or to differentiation between ice- and gas-phase ratios.

1.5   Goals of this Project

Using a numerical astrochemical model (described in detail in §2), this project aims to understand the difference between the gas-phase ammonia-to-water ratio in TW Hydra, as revealed by the Salinas et al. (2016) observation, and comets. While observational astronomy provides us with constraints, computational modeling allows us to probe the underlying processes. By replicating the physical and chemical environment in TW Hydra with a closed-box point-source model, we hope to determine the dependency of ammonia chemistry upon chemical and physical disk properties over the course of the disk lifetime. What superposition of physical and chemical parameters must exist to simultaneously support a low (~0.3–2%) ice-phase ratio and a high (~33–84%) gas-phase ratio? How does the chemistry evolve over time? What roles do ionizing radiation, grain-surface ammonia production, or initial chemical conditions play? How does chemistry vary in different locations in the disk? Which reactions are the most salient? This work seeks to answer these questions.

Chapter 2:
Methods

In this chapter, I will first outline the physical and chemical details of the 'global' model, from which the 'box' model used for this work is derived. I will then specify the characteristics and utility of the box model. I will motivate the selection of six disk locations for comparison with the box model throughout the project. Finally, I will describe the methods by which chemical reactions are traced from the models and used to understand chemical processes.

2.1   Global Model

The 0-D 'box' model that is used in this project, to be discussed in detail in §2.2, is derived from a 2-D 'global' model that couples chemical and physical processes in order to simulate the evolution of the disk's chemistry for a defined set of initial parameters, and includes a diverse range of chemical processes. This global model is in turn built upon the 2002 version of the Fortran numerical solver, DVODPK (Variable-coefficient Ordinary Differential equation solver with the Preconditioned Krylov generalized minimal residual method for the solution of linear systems) to solve differential equations representing the physical and chemical conditions of the disk. This solver was first incorporated into a 2-D 'global' chemical model by Jeffrey Fogel et al. (2011) to simulate the global chemical evolution of a vertical cross-section of a disk (an azimuthal slice extended in R and Z). The specific chemical model used in this work was an extension of the Fogel model, designed by Cleeves et al. (2015) in order to recreate the molecular ion chemistry of TW Hydra. The gas and dust distributions, gas and dust temperature, and ionizing radiation intensity within TW Hydra are represented by a physical model that was first formulated by Bergin et al. (2013) and also adapted by Cleeves et al. (2015). By investigating the effects of physical and chemical

properties simultaneously, the global model presents a comprehensive method to replicate both physical and molecular disk structure.

2.1.1 Physical Model

Gas and Dust Distribution

The total gas mass used in our model is $0.04 \pm 0.02 M_\odot$, based on *Herschel* observations of hydrogen deuteride (HD). HD is considered a superior gas tracer than CO because (1) CO is depleted in disks, (2) HD does not freeze-out due to its very low freeze-out temperature, and (3) HD is thought to exist at a constant ratio with H_2 throughout the disk. The total dust mass is calculated from the SED to be 4×10^{-4} $M_\odot$.

Dust grains in disks are known to coagulate and grow more massive over time, subsequently settling into the inner disk midplane (Furlan et al., 2006). The effects of dust settling are non-negligible; the loss of dust grains from the disk's upper atmosphere leads to a flatter disk in which radiation can penetrate further into the disk, thus increasing temperatures and ionization rates at lower Z and greater R. To roughly emulate this diversity of dust grain size and spatial distribution throughout the disk, two varieties of dust are included in the model: small grains with radii $r_g = 0.005 - 1 \mu m$ that are distributed vertically throughout the disk and large grains with radii $r_g = 0.005 - 1 mm$ that are concentrated to the disk midplane (low-Z). The actual sizes of the dust grains are distributed using the Mathis, Rumpl, & Nordsieck (MRN) grain size model, which scales abundance with radius like $n_g \propto r_g^{-3.5}$ (Mathis et al., 1977). Dust mass composition is assumed to be 80% silicate and 20% graphite. While the population of large dust grains constitutes 90% of the total dust mass, it is the small dust grains that dominate grain surface area and that are most influential for disk chemistry. Thus, radial concentration of large dust grains at smaller R due to settling (Andrews et al., 2012) is not taken into account in the global model, as it is the small grains that affect chemistry. Both large and small dust grains, as well as the gas,

are extended out to the outermost radius of 200 AU, which was estimated from observations of CO gas and light scattered from small dust in TW Hydra. Both the gas and dust density are shown in Figure 2.1.

The distribution of dust within TW Hydra is determined through the disk's spectral energy distribution (SED). (Andrews et al., 2012) Radial distributions, i.e. surface densities $\Sigma_{gas}(R)$ and $\Sigma_{dust}(R)$, of both the dust grains and the disk gas are described by power laws that diminish exponentially with increasing radius between 150 and 200 AU (as previously described in §1.1.2). From Cleeves et al. (2015), the dust grain surface density is

$$\Sigma_{dust}(R) = 0.04 \, \text{g cm}^{-2} \left(\frac{R}{R_c}\right)^{-1} \exp\left[-\frac{R}{R_c}\right] \tag{2.1}$$

. Vertical distributions, i.e. $\rho_{gas}(Z)$ and $\rho_{small\,dust}(Z)$, were set to be Gaussian:

$$\rho_{small\,dust}(R, Z) = \frac{(1-f)\Sigma_{dust}}{\sqrt{2\pi}Rh} \exp\left[-\frac{1}{2}\left(\frac{Z}{h}\right)^2\right] \tag{2.2}$$

$$\rho_{large\,dust}(R, Z) = \frac{f\Sigma_{dust}}{\sqrt{2\pi}R\chi h} \exp\left[-\frac{1}{2}\left(\frac{Z}{\chi h}\right)^2\right] \tag{2.3}$$

where f is the fraction of mass in large grains (0.9), χ is the scale height coefficient for large grains (0.2), and h is the scale height:

$$h(R) = 15\text{AU}\left(\frac{R}{R_c}\right)^{0.3} \tag{2.4}$$

where the critical radius R_c is 150 AU in both cases.

Temperature

Gas and dust temperatures vary greatly across the disk due to differential heating from accretion and the interaction of disk gas and dust with the various radiations sources affecting the disk. Dust temperatures are calculated using radiative transfer models that predict

22

variations in heating across the disk, as a result of both radiation from the central star and from outside of the disk, while assuming the dust is in radiative equilibrium. For TW Hydra, the TORUS radiative transfer code was used adopting a stellar effective temperature of 4110 K, the stellar mass 0.8 $M_\odot$, and the stellar radius 1.04 $R_\odot$. It is important to note that the gas and dust temperature are coupled in most regions in the disk, but the gas temperature can exceed the dust temperature in the high-Z surface regions due to lower gas and dust density and thus inefficient gas cooling. Temperature variations across the disk are shown in Figure 2.1.

Ionizing Radiation

The three main sources of ionizing radiation in TW Hydra are: cosmic rays, X-rays, and UV radiation. Each of these radiation types interacts uniquely in the disk, and the flux distributions of both X-ray and UV radiation are shown in Figure 2.1.These ionizing sources are crucial for the complex chemistry that takes place most frequently between ions within the disk.

Galactic cosmic rays, due to their high energies, are attenuated in the disk at a rate directly proportional to the vertical column density. In the case of TW Hydra, cosmic rays are thought to exist at significantly (orders of magnitude) lower flux within disks than in the interstellar medium, potentially due to the presence of stellar or disk winds (Cleeves et al., 2015).

X-rays emitted by the central host star are the dominant source of ionizing radiation at the disk surface. The X-ray signature of TW Hydra is well-studied due to the fact that the disks is oriented orthogonal to the line of sight; the X-ray luminosity is well-constrained (2×10^{30} erg cm^{-2} s^{-1}) and the star is known to periodically emit harder X-ray flares. While the X-ray flux is thought to be attenuated at greater depths within the disk, Igea & Glassgold (1999) introduce the possibility of non-negligible X-ray ionizations occurring in the disk midplane as a result of X-ray scattering within the outer layers.
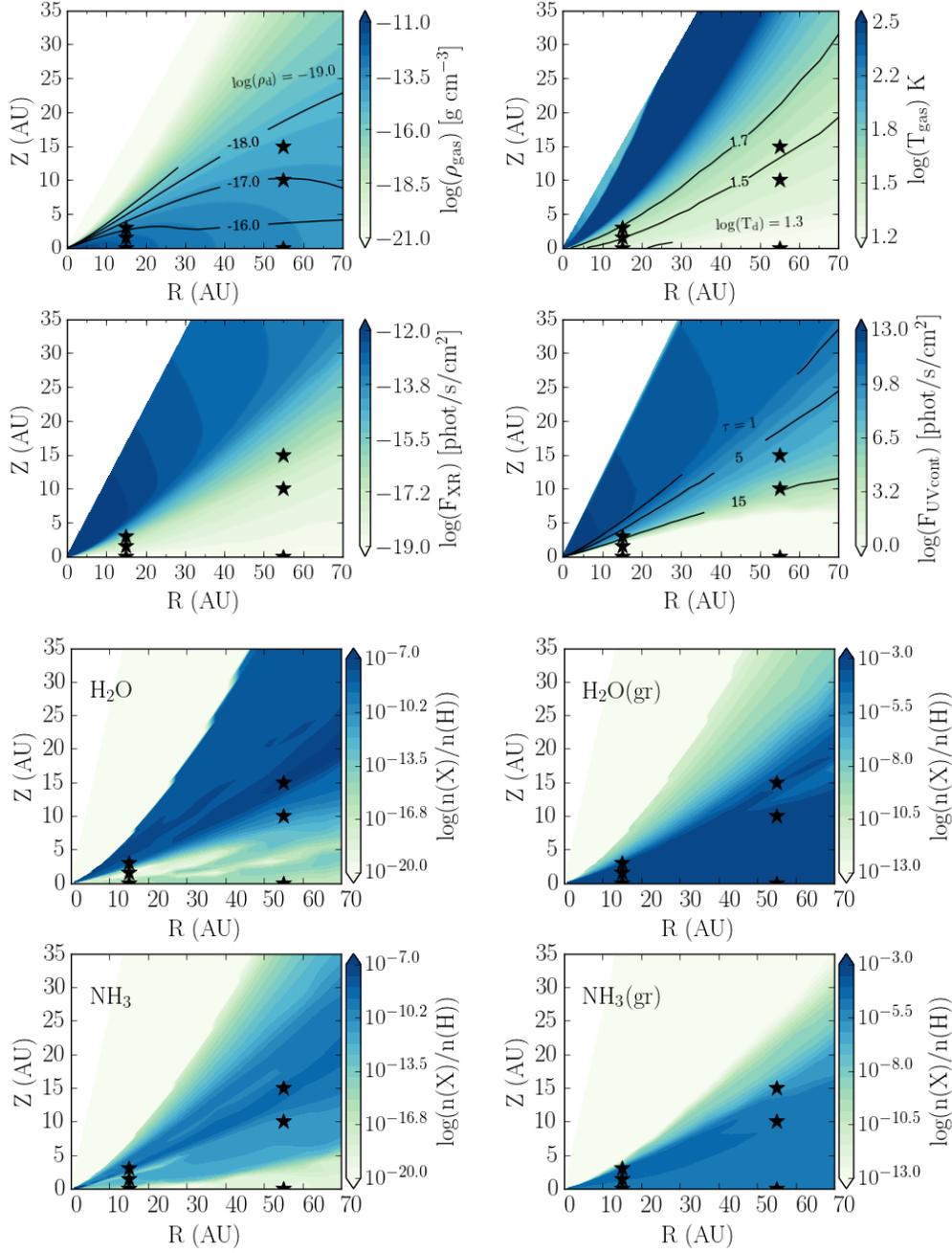
Figure 2.1: *First row:* Gas density distribution (left) and gas temperature distribution (right) in a TW Hydra-like protoplanetary disk across radius R and height Z. Contours in the density and temperature plots represent the distribution of dust density and temperature, respectively. *Second row:* Integrated X-ray flux between 1-20 keV (left) and λ-integrated UV flux (right) in a TW Hydra-like protoplanetary disk. Contour lines represent optical depth (First and second rows from Cleeves et al. (2015)). *Third and fourth rows:* Distributions of gas- and grain-phase H₂O (third) and NH₃ (fourth) in a TW Hydra-like disk at 1 Myr, as calculated by the global model. The six black stars denote the locations for this study, as discussed in §2.3.

UV radiation also plays an important role, originating both from the disk's host star and from the interstellar radiation field. Similarly to X-rays, UV flux has a significant ionizing presence at the disk surface, but is quickly depleted at inner and more distant (smaller Z, larger R) regions.

Finally, short-lived radionuclides, though known to be present in our own Solar System, were not included in this model due to TW Hydra's age and relative isolation from massive star forming regions.

2.1.2 Chemical Model

The chemical model employed for this study was first developed and used by Fogel et al. (2011) to model disk chemistry, via a modification of the ALCHEMIC code (Semenov et al., 2010). The main code is (1+1)-dimensional, i.e., a 1-D code that is calculated over height for a given radius that is then reiterated across a range of radii (note that this dimensionality eliminates the possibility of modeling radial interactions). However, the UV field is calculated across a proper two-dimensional cross-section of the disk (Fogel et al., 2011). The model includes 6284 chemical reactions from the OSU gas-phase network (Smith et al., 2004), including the following reaction types: neutral-neutral, ion-neutral, ion recombination, freeze-out, thermal desorption, non-thermal desorption, photodissociation, photoionization, charge exchange, X-ray induced UV photons, CO self-shielding, H_2 self-shielding, and formation of water and H_2 on grain surfaces. Only reactions including up to two reactants were included. Previous works, including Cleeves et al. (2014a) and Cleeves et al. (2015), added to this reaction network by incorporating deuterium reactions, self-shielding of HD and D_2, and 77 additional grain surface reactions (including NH_3). It is important to note the uncertainty inherent in the model due to the fact that only a portion of the included reaction rates have been verified through laboratory experiments.

The numerical code calculates chemical abundances over time by solving differential rate

equations of the basic form

$$\frac{dn(i)}{dt} = \sum_j \sum_l k_{jl} n(j) n(l) - n(i) \sum_j k_{ij} n(j) \qquad (2.5)$$

in which the first term describes the positive change in abundance of some molecule i due to all production reactions with reactants j and l ($j + l \rightarrow i + ?$) that occur with rate k_{jl} and the second term describes the negative change in abundance of i due to all destruction reactions with reactants i and j ($i + j \rightarrow ?$) that occur with rate k_{ij}. However, many reaction types are included in the code that cannot be modeled by the interactions of two molecules, including photodissociation, self-shielding, adsorption, and desorption. In addition, a two-step procedure was developed for grain surface chemical processes. For each such reaction type that is not incorporated in the OSU database, the reaction rate k is uniquely determined as described below.

Light-matter Interactions

Photodissociation is the breaking up of a free (gas-phase) molecule into its component atoms or molecules upon interaction with a photon. Photodissociation reactions were included in the model for molecules with both known (van Dishoeck, 2006) and unknown UV photodissociation cross sections (where the cross section is an approximate representation of the probability of a photodissociation event). The rates for each case are

$$k_{photodissociation,\, known} = \int \frac{4\pi\lambda}{hc} \sigma(\lambda) J_\lambda(r, z) d\lambda \mathrm{s}^{-1}, \qquad (2.6)$$

where $\sigma(\lambda)$ is the cross section as a function of wavelength and $J(r, z)$ is the radiation flux at a specific (r, z) in the disk, and

$$k_{photodissociation,\, unknown} = G_0 (100 \text{ AU}) \left(\frac{100.0}{R(\mathrm{AU})} \right)^2 \times \alpha \frac{J_{\lambda,z}}{J_{\lambda,z_{max}}} (r, z, \lambda = 1500 \text{ Å}) \mathrm{s}^{-1} \qquad (2.7)$$

where the radiation field scaling factor between the interstellar field and the model $G_0(100$ AU$) = 700$, α is the unshielded photodissociation rate as listed in the UMIST 2006 database (Woodall et al., 2007), and the ratio of J is the radiation field attenuation.

In addition, self-shielding of CO and H_2 were incorporated into the model. Both H_2 and CO are photodissociated only by specific frequencies of radiation via line absorption. As radiation enters a cloud of H_2 or CO, the specific ionizing frequencies will be quickly absorbed by the outer layers of the gas, effectively shielding the molecules that reside deeper within. Rates of self-shielding reactions were calculated following the work of Visser et al. (2009) and Lee et al. (1996).

Gas-grain Interactions

In addition to these photon-molecule interaction, gas-grain interactions were also included in the model. In gas-grain interactions, adsorption is the process by which gas-phase molecules become stuck (frozen) to dust grains, and desorption is the opposite process by which a frozen grain-phase molecule is freed from a dust grain to become a gas-phase molecule. In order to account for the chemical effects of gas-grain interactions, both adsorption and desorption processes were included in the code. The reaction rate for adsorption is

$$k_{adsorption} = \sigma_{gr} \sqrt{\frac{8.0 k_B T}{\pi \beta m_H}} S \, n_{gr} (\text{s}^{-1}) \tag{2.8}$$

where σ_{gr} is the dust-grain cross section, πr_{gr}^2, β is the molecular weight of the gas-phase molecule, and S is the sticking coefficient for gas-grain collisions (assumed to be 1 for low temperatures). Three different varieties of desorption reactions were incorporated into the model: thermal desorption, cosmic ray desorption, and photodesorption. In the case of thermal desorption, the desorption rate was determined from the Polyani-Wagner relation such that

$$k_{thermal\,desorption} = \sqrt{\frac{3.0 \times 10^{15} k_B E_b}{\pi^2 \mu m_H}} e^{-E_b/T} (\text{s}^{-1}) \tag{2.9}$$

where E_b is the binding energy of the molecule to the grain and T is the grain temperature. The desorption rate for cosmic ray desorption was determined by Hasegawa & Herbst (1993) and Bringa & Johnson (2004). Finally, the desorption rate for UV photodesorption is

$$k_{photodesorption} = F_{UV} Y \frac{\sigma_{gr}}{N_{sites}} \alpha_{mono} \qquad (2.10)$$

where F_{UV} is the total wavelength-integrated UV flux, Y is the number of particles freed from the grain surface per UV photon (the yield; 10^{-3} except for CO and H_2O), N_{sites} is the total number of potential reaction sites (i.e. molecules) on the grain surface (assumed to be 10^6), and α_{mono} is the correction factor for grains with deposits more than two monolayers thick:

$$\alpha_{mono} = \frac{N_p n(i)}{n_{ice} N_m} \qquad (2.11)$$

where $N_p = 2$ corrects for the penetration of UV photons only through the uppermost monolayers of the grain molecules, $n(i)$ is the abundance of the desorbing molecule on the grain surface, n_{ice} is the total abundance of all molecules on the grain surface, and N_m is the total number of monolayers on the grain.

Grain Surface Interactions

The model also incorporates 77 grain-surface reactions that occur between frozen ice-phase molecules. The formation processes of $H_2/HD/D_2$, H_2O/HDO, H_2CO, CH_3OH, CH_4, CO, CO_2, N_2, N_2H_2, HNO, NH_3, HCN, OCN, and H_2CN on grains are included. As established by Hasegawa et al. (1992), the rate of on-grain reactions between two frozen species i and j is represented by:

$$k_{ij,grain} = \frac{\kappa_{ij}(R_{diff,i} + R_{diff,j})}{n_d} \qquad (2.12)$$

in which κ_{ij} is the probability that a reaction occurs when two molecules encounter one another (determined by reactions' activation energy), n_d is the number density of dust grains, and R_{diff} is the diffusion rate of a particle 'sweeping' across a grain surface by thermal

hopping. R_{diff} is in turn calculated to be $1/t_{diff}$. In this model, the diffusion time t_{diff} is the time for a single particle on a grain surface to 'hop' (due to thermal energy) across the entire grain surface. t_{diff} is calculated to be

$$t_{diff} = N_s t_{hop} \tag{2.13}$$

where N_s is the number of particle sites on a grain (approximated to 10^6) and t_{hop} is the time for a particle to undergo one thermal hop and migrate from one on-grain site to another. Finally, the hopping time t_{hop} is determined to be:

$$t_h op = \nu_0^{-1} \exp E_b/kT_d \tag{2.14}$$

where ν_0 is the characteristic vibration frequency of the adsorbed particle, E_b is the potential energy barrier between on-grain sites, and T_d is the dust temperature (Hasegawa et al., 1992).

Due to imperfect representations of grain settling and growth, the timescales returned by the chemical model do not necessarily align with actual timescales in TW Hydra. Over time, both grain growth and grain settling deplete the total grain surface area that is available for complex molecular interactions in the disk. As a result, in disks many chemical reactions and processes take place at an increasing slower rate, especially in the outer disk layers that loose grains due to settling. However, as our model does not evolve dust grain size or distribution with time, we instead assume that results of the chemical model occur on faster timescales than in reality. Taking this into account, steady-state values for TW Hydra are evaluated from the model at 1 Myr, to chemically match the disk's estimated age of 3-10 Myr (Cleeves et al., 2015).

2.2 Box Model

The primary tool used in this work is a one-dimensional 'box' model that simulates the local chemical evolution of a specific point in R and Z within the disk. While the global model is used to observe and simulate the physics and chemistry of entire disk systems, the box model is used to rigorously examine points within a disk.

This local model recreates the chemical evolution of an environment with specified constant physical and chemical conditions, namely gas density, gas and dust temperature, UV flux, cosmic ray flux, X-ray flux, and initial molecular composition. While these parameters are calculated for each location in the disk within the global model, they are specified by the user in the box model, allowing for tests of any combinations of parameters. Compared to the comprehensive global model the box model, which takes hours to complete a computation with 100 log-time steps over 10 million years, the box model takes just seconds to minutes to complete the same computation with 1000 log-time steps. Thus, this code is optimal for quick and local tests, and when paired with data from larger models that specify the physical and chemical conditions at various locations at the disk, enables an extremely detailed investigation of molecular processes at specified disk locations.

Table 2.1: Physical parameters available for user manipulation in the Box Model

Name	Units	Description
Gas Temperature	K	Temperature of gas-phase molecules
Dust Temperature	K	Temperature of dust grains and grain-phase molecules
Gas Density	g/cm^3	Volume density of H_2 gas at disk location
Cosmic Ray Rate	ionizations/s/H_2	Flux of cosmic rays at the disk surface
Vertical Column Density	$N(H_2)/cm^2$	Measure of depth within disk, used to attenuate CR Flux
UV Flux	photons/cm^2/2	Flux of UV photons at disk location
X-Ray Rate	ionizations/s/H_2	Flux of X-rays at disk location

Compared to that of the global model, the physical model used in the box model is simpler due to the higher degree of user control. As shown in Table 2.1, gas density, gas

temperature, dust temperature, UV flux, and X-ray flux are all values directly provided to the model by the user. The exception to this rule is the attenuated cosmic ray rate, which is calculated within the model based on an unattenuated rate and a vertical column density. All of these aforementioned parameters that are supplied to the box model, except in cases of experimentation, are taken directly from the output of the global model (described in detail in §2.1). The initial abundances of all molecules in the box model, as well as the abundances (density) of dust grains, are also explicitly established by the user. Finally, dust grain size is set at a constant value that does not change over the lifetime of the disk, nor does the grain density change over time to simulate the effects of grain settling.

2.3 Model Location Selection

By referring to the output of the global model, the input parameters for the box model can be determined at a given location in the disk. Six box model locations were chosen after examining the global model distributions of NH_3 and H_2O in both gas-phase and ice-phase throughout the disk. Locations were selected at regions with (1) peak gas-phase abundances, corresponding to higher-Z locations near the disk surface, (2) peak ice-phase abundances at

Table 2.2: Physical parameters for six locations of interest in the disk

	Inner Surface	Inner Transition	Inner Midplane	Outer Surface	Outer Transition	Outer Midplane
Radius (AU)	15	15	15	55	55	55
Vertical Height (AU)	3	1.5	0	15	10	0
Gas Temperature (K)	49	33	23	34	27	13
Dust Temperature (K)	49	33	23	34	27	13
Gas Density (g/cm^3)	4.7×10^{-14}	3.9×10^{-13}	8.1×10^{-13}	3.2×10^{-15}	1.0×10^{-14}	2.8×10^{-14}
Cosmic Ray Rate (ionizations/s/H$_2$)	2.0×10^{-17}	2.0×10^{-17}	2.0×10^{-17}	2.0×10^{-17}	2.0×10^{-17}	2.0×10^{-17}
Vertical Column Density (N(H$_2$)/cm^2)	4.1×10^{22}	7.3×10^{23}	3.9×10^{24}	1.6×10^{22}	1.1×10^{23}	9.3×10^{23}
UV Flux (photons/cm^2/2)	4.3×10^8	9.8×10^{-12}	0	2.1×10^8	2.7×10^5	0
X-Ray Rate (ionizations/s/H$_2$)	1.6×10^{-16}	2.0×10^{-18}	6.5×10^{-20}	3.6×10^{-17}	1.3×10^{-18}	1.1×10^{-19}
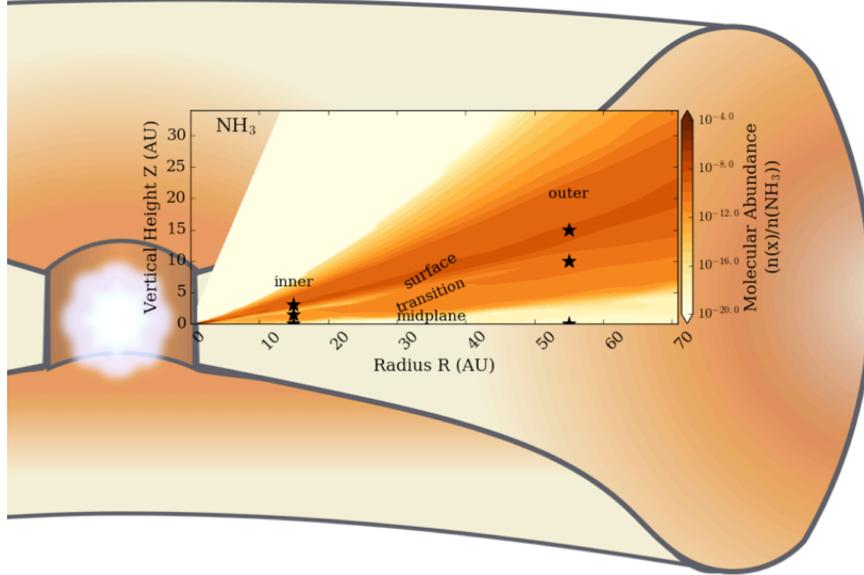
Figure 2.2: Model representation of ammonia distribution in a TW Hydra-like system. Black stars represent the six locations examined in this work.

low-Z locations within the disk midplane, and (3) non-peak abundances in both the ice- and gas-phase at intermediate locations vertically between the surface and midplane. In addition, locations were selected for both the inner and outer disk, at 15 and 55 AU, in order to examine how radial distance affects ammonia and water chemistry. The six locations that were ultimately chosen to analyze are listed in Table 2.2 and are superimposed on the gas- and grain-phase abundance maps of NH_3 and H_2O in Figure 2.1.

2.4 Tracing Reactions

One powerful elements of the box model code is that it outputs, for each log-time step, the rates of every reaction that has taken place. This allows the user to trace how the impact of a reaction changes with time, as well as determine which reactions are driving the abundance of a particular molecule. This inductive tool enables the investigation of molecular processes. By tracing back reactant to reactant to reactant, one can define the chains and networks of reactions that take place to create a specific molecule. Additionally, by analyzing how reactions speed up or slow down versus time, the causes of chemical changes can be pinpointed.

In this way, the box model provides general insight into how molecules form, and specific insight into what processes are occurring within protoplanetary disks. An example output of the rate-printing function of the code, including the reactants, products, reaction rate, and abundances of the reactants and products, is shown in Figure 2.3.

```
Printing rate results for t = 0.1 Myr.
[ID:  5939] Rate:  1.140e-08   R1,R2: OH(gr)      + H2CO(gr)    -->    HCO(gr)    + H2O(gr)
            OH(gr)     : 8.596e-25
            H2CO(gr)   : 1e-05
            HCO(gr)    : 1.176e-12
            H2O(gr)    : 0.0002513
[ID:  4759] Rate:  9.710e-09   R1,R2: H2O         + GRAIN       -->    H2O(gr)    + GRAIN
            H2O        : 1.524e-11
            GRAIN      : 6e-12
            H2O(gr)    : 0.0002513
            GRAIN      : 6e-12
[ID:  5331] Rate: -4.940e-09   R1,R2: H2O(gr)     + LYAPHOTON   -->    OH         + H
            H2O(gr)    : 0.0002513
            LYAPHOTON  : N/A
            OH         : 1.733e-11
            H          : 3.715e-11
```
                                                                                          S

Figure 2.3: A portion of an example output of the box model code. For each reaction ID, the reaction rate is provided as well as the reaction equation. The abundances of all reactants and products involved are listed below each reaction. Reactions are listed in order of descending rate.

Chapter 3:
Fiducial Model Results

This chapter presents the box model results for the configuration of parameters that we define as the fiducial model. The input physical parameters are unchanged from those output by the global model (as listed in Table 2.2), all initial chemical abundances were unchanged from the model used by Aikawa & Herbst (1999) (as listed in Table 3.1), and the formation of ammonia on grains is included. The chemical results of the fiducial box model at the six locations are shown in Figure 3.1. The global and local characteristics of these results are discussed here.

3.1   Global Characteristics

In the entirety of the disk, both ammonia and water exist predominantly in the grain phase, while being present at lower abundances in the gas-phase. These abundances reflect the adsorption, or freeze-out, of gas-phase molecules onto dust grains due to the low temperatures present throughout the disk. Ammonia freezes out at around ~ 60 K and water freezes out at around ~ 100 K, and the temperature of the test locations in the disk ranges only from 14–49 K, always below the freeze-out temperature. However, not all gas-phase NH_3 and H_2O are frozen onto grains because (1) there is a delay between the formation of a gas-phase molecule and its adsorption onto a grain (i.e. freeze-out is not instantaneous) and (2) frozen molecules are

Table 3.1: Initial molecular conditions for fiducial box model. From Aikawa & Herbst (1999) Fig. 5a.

Name	Abundance $(n(X)/n(H))$
H_2	5.00×10^{-1}
$H_2O(gr)$	2.00×10^{-4}
O	1.00×10^{-8}
O_2	1.00×10^{-8}
He	1.40×10^{-1}
N	2.25×10^{-5}
N_2	2.25×10^{-5}
CN	6.00×10^{-8}
H_3^+	1.00×10^{-8}
S^+	1.60×10^{-6}
Si^+	1.60×10^{-9}
Mg^+	3.00×10^{-8}
Fe^+	2.00×10^{-8}
CO	6.00×10^{-12}
C	5.00×10^{-9}
NH_3	8.00×10^{-8}
HCN	2.00×10^{-8}
C^+	1.00×10^{-10}
HCO^+	9.00×10^{-9}
C_2H	8.00×10^{-9}
Grain	6.00×10^{-12}
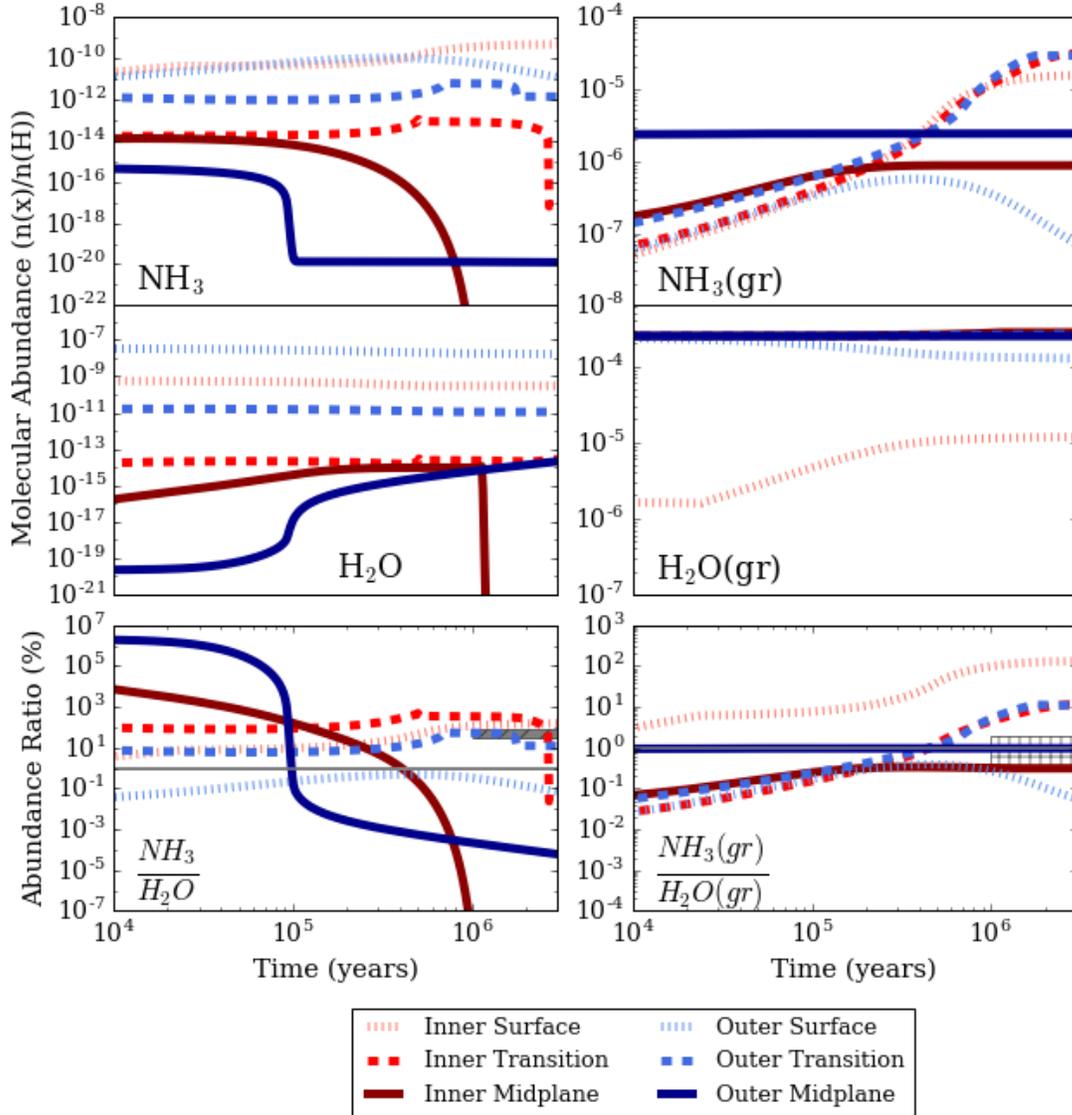
Figure 3.1: Model evolution of gas- and grain-phase ammonia (NH₃) and water (H₂O) abundances and ratios over the chemical lifetime of the TW Hydra-like protoplanetary disk (1×10^4 to 3×10^6 years). Plots at left show gas-phase trends while the plots at right show grain-phase trends. The upper four plots represent molecular abundances while the bottom two represent abundance ratios (where the solid gray lines represent a ratio of 1%). Different locations in the disk (as described in Table 2.2) are denoted by different line colors and patterns: red corresponds to the inner disk (R = 15 AU) while blue corresponds to the outer disk (R = 55 AU); dotted lines represent the photon-dominated and peak-abundance surface layers (Z = 3 AU and Z = 15 AU), dashed lines represent the transitionary region between surface and midplane (Z = 1.5 AU and Z = 10 AU), and solid lines represent the shielded midplane (Z=0 AU). Dark diagonal hatching represents the Salinas et al. (2016) gas-phase ratio; light crossed hatching represents the Mumma & Charnley (2011) cometary ice ratio.

freed from grains via photodesorption by ionizing UV radiation, X-ray radiation, or cosmic rays.

It is in part because of the effects of radiation that gas-phase abundances increase for regions at higher Z; for both ammonia and water, the exposed surface presents the highest gas-phase abundances, followed by the transition region, and the shielded midplane has the lowest gas-phase abundances. The same stratification is not present for ice-phase abundances.

Throughout the disk, there is a greater abundance of water and water ice compared to ammonia and ammonia ice, respectively, as a result of the initial molecular conditions. The reservoir of hydrogen gas is available for the production of both NH_3 and H_2O, with hydrogen present in an abundance 3–4 orders of magnitude greater than either nitrogen or oxygen. However, the initial disk chemistry has ~6 times more oxygen than nitrogen. In addition, almost of the oxygen reservoir exists in the form of $H_2O(gr)$, while only a fraction of the nitrogen reservoir exists as $NH_3(gr)$ (see Fig. 3.1). These conditions allow for a greater abundance of water compared to ammonia that is maintained in the disk across space and time.

Finally, it is important to note that chemical abundances evolve during the lifetime of the disk. Referring to Figure 3.1, gas-phase and ice-phase ammonia at the inner disk surface increase two orders of magnitude over the lifetime of the disk; ice-phase water increases by almost one order of magnitude; and gas-phase abundances of both molecules in the midplane fluctuate by over 6 orders of magnitude. Disk chemistry evolves as the disk evolves.

3.2 Local Characteristics

The chemical effects of radial distance to the star are evident when comparing the inner locations with the outer locations. Referring again to Figure 3.1, while there is more gas-phase ammonia and water in the outer (55 AU) transition region than the inner (15 AU)

transition region, owing to the lower densities and thus decreased rate of freeze-out in the outer disk, this is not the case everywhere. In the midplane, the trend is flipped; gas-phase NH_3 and H_2O abundances before ~1 Myr are higher in the inner midplane than the outer midplane. At the surface, gas-phase H_2O shows higher abundances at 55 AU than 15 AU, while gas-phase NH_3 shows equal abundances at both radii until ~0.3 Myr, when the inner surface abundance rises above the outer. In the ice-phase, $NH_3(gr)$ is more abundant in the outer than inner midplane, though grain-phase abundances are equal for both radii in the transition regions, and grain-phase abundances follow a similar trend to the gas-phase (inner abundance overtaking outer at ~0.3 Myr) at the surface. Ice-phase water stays constant around 10^{-4} $n(H_2O(gr))/n(H)$ at most disk locations, though it shows variation at the surface, dropping 1–2 orders of magnitude at the inner surface. Each of these comparisons demonstrate that the location within the disk affects local ammonia and water chemistries.

Multiple changes in abundance with time are present in the midplane. These changes affect both gas-phase ammonia and water. As shown in the upper left panel of Figure 3.1, gas-phase ammonia is depleted by almost 5 orders of magnitude in the outer midplane before 0.1 Myr, and by almost 10 orders of magnitude in the inner midplane before 1 Myr, due to the freeze-out of gas-phase ammonia onto grains. Gas-phase water also experiences a drop-off in the inner midplane, quickly decreasing by 10 orders of magnitude around 1 Myr immediately after the depletion of gas-phase ammonia. In the outer midplane, however, gas-phase water experiences an increase of over 5 orders of magnitude around 0.1 Myr, concurrently with the drop in gas-phase ammonia. In the ice-phase, $NH_3(gr)$ increases in by approximately one order of magnitude in the inner midplane before 1 Myr, concurrently with the gas-phase NH_3 decrease.

Outside of the midplane and closer to the surface, changes with time are less severe. NH_3 gas decreases at the outer surface and increases at the inner surface around 1 Myr, but only by 1–2 orders of magnitude. Concurrently, grain-phase $NH_3(gr)$ behaves similarly, decreasing at the outer surface and increasing at the inner surface around 0.3 Myr by 1–

2 orders of magnitude. Water ice also experiences a slow increase of almost one order of magnitude in the inner surface between 0.01 and 1 Myr.

In the transition regions, water and water ice abundances remain constant over time. However ammonia gas experiences a 1 order of magnitude rise, plateau, and fall between 0.1 and 3 Myr in both the inner and outer transition regions. Ammonia ice experiences a steady rise over the disk lifetime, increasing from 10^{-7} $n(NH_3(gr))/n(H)$ at 0.01 Myr to almost 10^{-4} $n(NH_3(gr))/n(H)$ at 3 Myr.

These data suggest that (1) distinct disk regions exhibit distinct ammonia and water chemistries, and (2) ice- and gas-phase chemical processing over 3 Myr can alter NH_3 and H_2O chemistries from their inherited initial abundances. We report a high (~10^2) gas-phase NH_3/H_2O ratio occurring only in the surface and transition regions of disks, and a low (~1) ice-phase $NH_3(gr)/H_2O(gr)$ ratio occurring in the disk midplane.

However, questions remain regarding the roles played by independent disk processes. The following three chapters report the results of the box model after variations in grain-phase chemistry, ionizing radiation, and chemical inheritance of ammonia.

Chapter 4:
Gas- & Grain-Phase NH$_3$ Chemistry

Ammonia can be formed via two pathways: through interactions between free molecules in the gas phase, and through interactions between molecules frozen onto dust grains in the grain phase. To investigate the contributions of the two pathways to the ammonia reservoirs in TW Hydra, the code was run again under the fiducial physical conditions and chemical abundances (as defined in Tables 2.2 and 3.1), but removing the following three hydrogenating equations that constitute the grain-phase production of NH$_3$(gr) from H(gr) and N(gr):

$$H(gr) + N(gr) \rightarrow NH(gr), \tag{4.1}$$

$$H(gr) + NH(gr) \rightarrow NH_2(gr), \tag{4.2}$$

$$H(gr) + NH_2(gr) \rightarrow NH_3(gr). \tag{4.3}$$

The resulting NH$_3$ and NH$_3$(gr) abundances and the corresponding ammonia-to-water ratios are presented in Figure 4.1. The exclusion of grain surface ammonia formation did not lead to any variation in the abundances of water or water ice. Furthermore, the abundances of NH$_3$ and NH$_3$(gr) remained almost completely unchanged at the disk surface and in the transition region. In the midplane, however, where ice-phase chemistry dominates, both gas- and grain-phase ammonia chemistry were significantly affected. In the outer midplane, the gas-phase ammonia abundance increased by 5 orders of magnitude while the total (gas-phase + grain-phase) ammonia abundance decreased by 2 orders of magnitude in the absence of grain surface formation. Additionally, the grain-phase ammonia abundance in the outer midplane is no longer constant, but rather slowly increasing over time. In the inner midplane, like in the outer midplane, the total (gas- + grain-phase) ammonia abundance in the inner
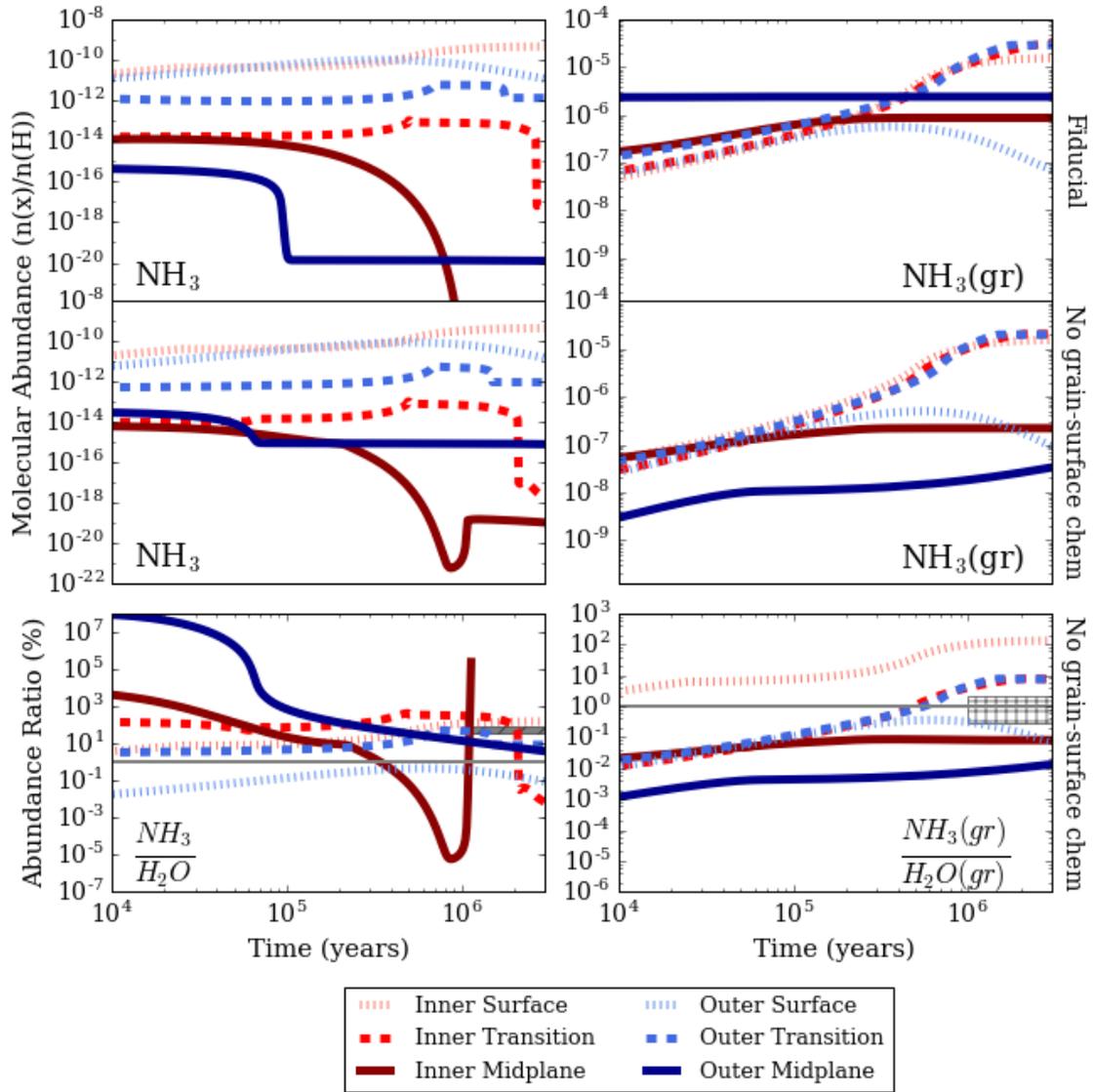
Figure 4.1: Same as Figure 3.1, with the second and third row of plots showing results without the formation of ammonia on grains.

midplane dropped by a factor of 3 in the absence of grain surface formation.

The decrease in grain-phase $NH_3(gr)$ abundance in the inner and outer midplane in the case without grain surface chemistry can be easily explained. The formation of $NH_3(gr)$ on grains has been restricted from two mechanisms to one, and so $NH_3(gr)$ can now only form as gaseous NH_3 freezes out. The freeze-out mechanism is markedly slower than freeze-out combined with grain surface formation, and so the ice abundance develops more slowly, and never reaches the NH_3 abundance achieved in the fiducial case.

However, the gas-phase results in the outer midplane are surprising, as they show the gas-phase ammonia abundance increasing after one of the formation pathways has been removed. One might expect the transition from two formation pathways to one might align with a decrease in the amount of gas-phase ammonia that is produced, as was shown in the ice-phase. This is not the case, and the cause of the increase in gas-phase NH_3 is not immediately intuitive. However, the cause can be deduced from examining the intermediary molecules (e.g. NH, NH_2, NH(gr), $NH_2(gr)$) and individual steps of grain-surface ammonia
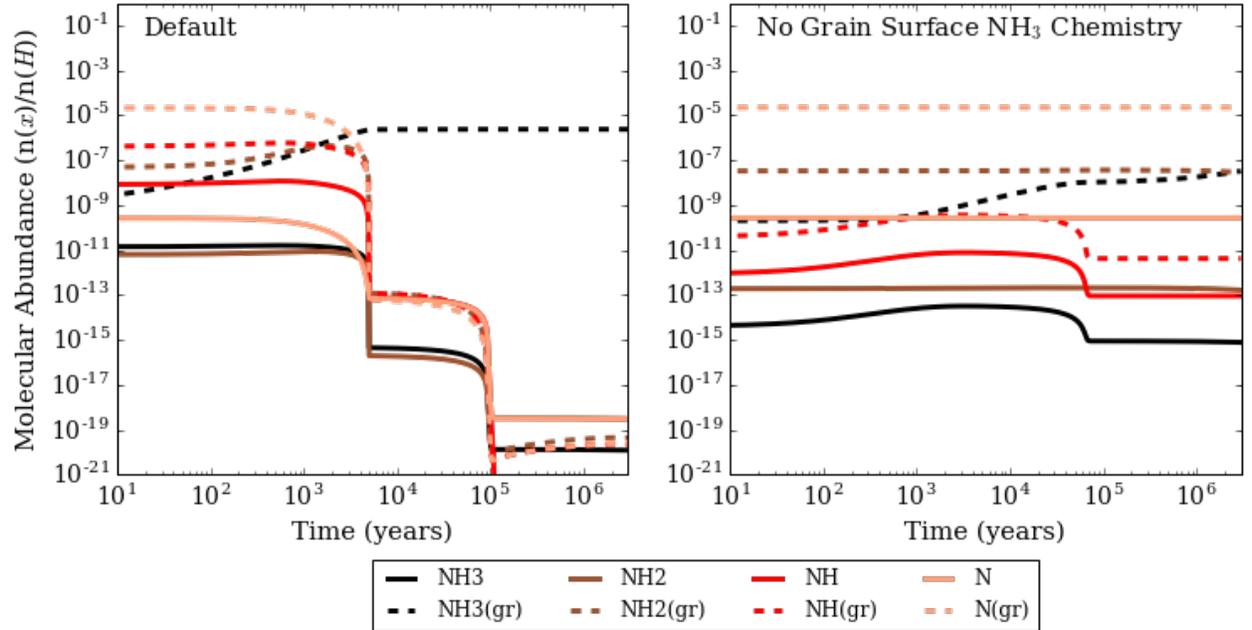
Figure 4.2: Molecular abundance of NH_3, NH_2 and NH in the outer (55 AU) midplane (Z = 0) in the gas and grain phase across the disk lifetime in the fiducial case (left) and the case without grain surface formation of $NH_3(gr)$ (right). Gas-phase molecules are represented by solid lines; their grain-phase companions are represented by dashed lines.

formation.

While grain-surface formation does lead to more efficient production of ammonia on grains, it also stifles the formation of gas-phase ammonia (see Figure 4.2). The formation of $NH_3(gr)$ and $NH(gr)$ on grains is more efficient than the desorption of $NH_2(gr)$ and $N(gr)$, respectively (interestingly, the same is not true for the formation of $NH_2(gr)$ by $NH(gr)$). Thus, if $NH_2(gr)$ or $N(gr)$ are present on grains, they are ~100 times more likely to bind with $H(gr)$ to form $NH_3(gr)$ or $NH(gr)$ than to desorb into NH_2 or N. This leads to a runaway process in which nitrogen becomes trapped on grains through the relentless formation of $NH_3(gr)$. When grain surface chemistry is eliminated, gas- and grain-phase N and NH_2 cannot be hydrogenated into $NH_3(gr)$, and the trapping of nitrogen on grains in the form of $NH_3(gr)$ is slowed. Furthermore, the additional N and NH_2 present in the disk due to desorption of the $N(gr)$ and NH_2 lead to continued gas-phase production of NH_3 that counters freeze-out, leading to a greater final ammonia abundance. These processes are shown in Figure 4.2.

The same difference is not observed in the transition and surface regions as $NH_2(gr)$, $NH(gr)$, and $N(gr)$ are over 10 orders of magnitude less abundant there, and thus their effects on the production of $NH_3(gr)$ are essentially negligible.

Chapter 5:
Effects of Ionizing Radiation

Many chemical reactions in protoplanetary disks are driven by the catalyzing effects of electric attraction between charged ions and neutral molecules. These ions are formed due to interactions with radiation, predominantly X-rays and ultraviolet radiation (UV) from the central star and cosmic rays (CR) from galactic sources, as explained in §2.1.1. To investigate how the ammonia-to-water ratios throughout TW Hydra are affected by these ionization sources, the code was run again under fiducial physical conditions (again, as defined in Tables 2.2 and 3.1) but with radiation sources removed in the following permutations: no CR, no UV, no X-rays, no CR or UV, no CR or X-rays, no UV or X-rays, no CR or UV or X-rays. To facilitate easier interpretation of this 8×6 data set, we present the gas-phase ammonia-to-water ratios only for the gas-rich surface and transition regions, and we present the ice-phase ratios only for the ice-dominated midplane regions (see Figure 5.1, upper and lower two rows, respectively).

As shown in Figure 5.1, the gas-phase ratio remains almost unchanged across the disk for the case without only X-ray radiation, but changes significantly in some regions in the absence of UV or cosmic rays. Observing the outer transition region, the ratio decreases by over 2 orders of magnitude in the absence of cosmic rays, increases by 1 order of magnitude in the absence of UV rays, and remains close to the fiducial case when both UV and CR are absent. A similar trend is present in the inner transition region, where the ratio becomes negligible for any case lacking cosmic rays. The removal of UV radiation at the disk surface depletes gas-phase water and thus increases the gas-phase ammonia-to-water ratio. Taken together, these results show that (1) UV radiation depletes the NH_3/H_2O ratio and (2) cosmic rays increase the NH_3/H_2O ratio.

In the case without any ionizing radiation sources, we deemed the gas-phase ratios incon-
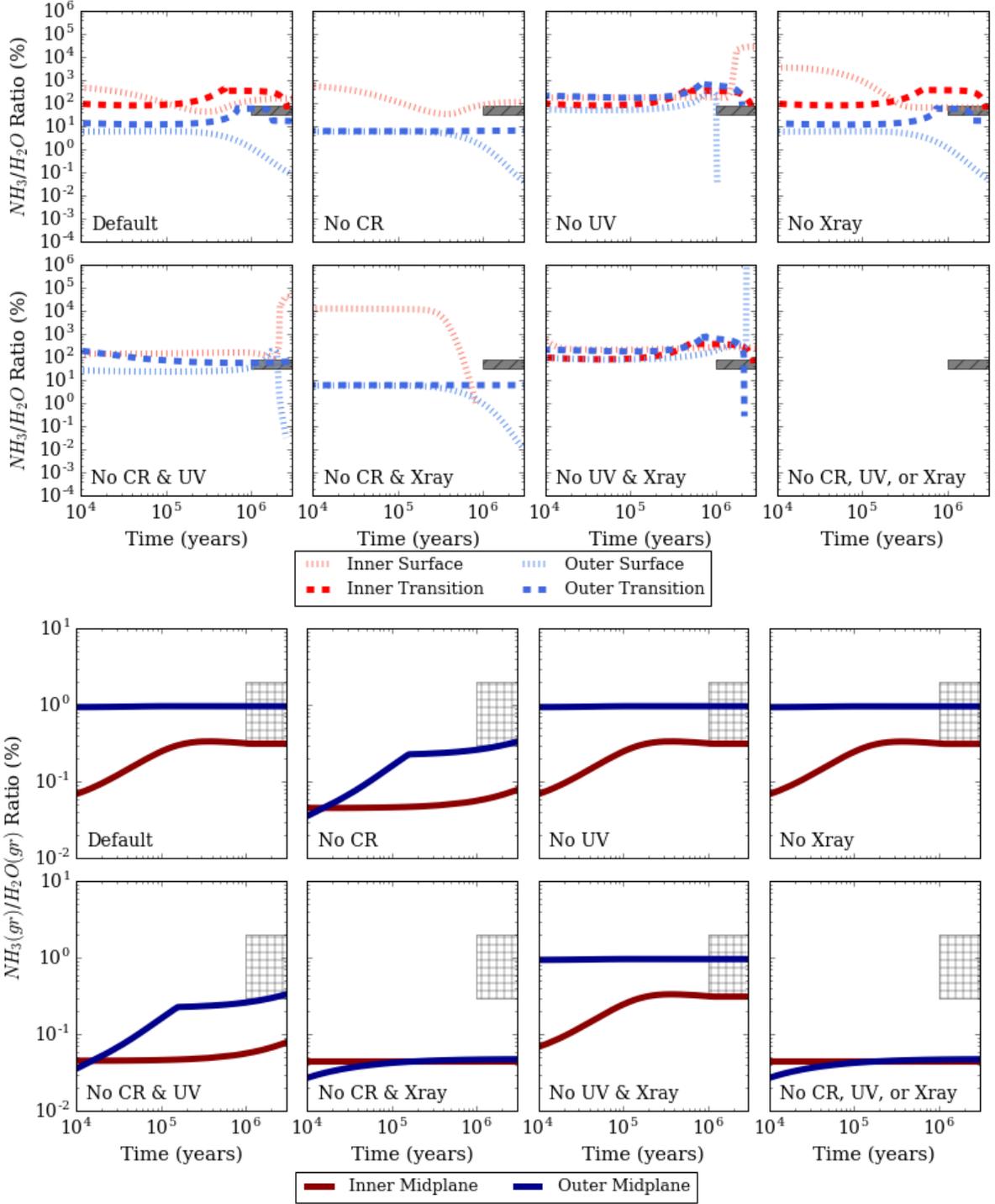
Figure 5.1: *(Above)* Evolution of gas-phase ammonia-to-water ratios over the chemical lifetime of the disk model for various combinations of ionizing radiation sources (X-rays, cosmic rays, and ultraviolet rays). Different locations in the disk are denoted by different line colors and patterns, as in Figure 3.1. Only surface and transition regions are shown as gas reservoirs are negligible in the midplane. Ratio curves are truncated or omitted if the abundances of either NH_3 or H_2O drop below 1×10^{-15} n(X)/n(H). Dark diagonal hatching represents the Salinas et al. (2016) result. *(Below)* Same as above, but presenting the ice-phase ammonia-to-water ratios in the ice-dominated midplane. Light crossed hatching represents the Mumma & Charnley (2011) cometary ice result.

clusive, because the abundances of both ammonia and water fall below $10^{-15} n(X)/n(H)$.

The ice-phase ratios as shown in Fig. 5.1, in contrast, undergo less variation due to the attenuation of radiation in the midplane. Indeed, the NH_3/H_2O ice ratios remain almost identical to the fiducial case in the absence of UV, X-rays, and UV & X-rays. The removal of cosmic rays, which are capable to penetrate through the outer layers of the disk and thus are present in the shielded midplane, leads to a significant decrease in the ratio by a factor of ~3 in both the inner and outer midplane. Finally, if both cosmic rays and X-rays are removed, the ice ratio is further depleted to approximately one order of magnitude less than the fiducial case.

In Figure 5.2, we take a closer look at the ionizing sources and processes that affect ammonia and water chemistry in the outer transition region. It is immediately evident that, while gas-phase ammonia is coupled to the presence of cosmic rays, gas-phase water is coupled to ultraviolet radiation. It also becomes clear that the slight increase in NH_3 abundance occurring around 1 Myr is tied to cosmic rays. Indeed, the production of ammonia is largely driven by the following reaction:

$$H_3^+ + N_2 \rightarrow N_2H^+ + H_2 \tag{5.1}$$
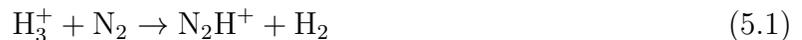
where ionized molecular hydrogen in the form of H_3^+ interacts with bulk molecular nitrogen in the form of N_2 to produce N_2H^+, a key molecule in the ammonia production chain. Most interestingly, H_3^+ is formed primarily from H_2^+, which is in turn formed primarily by the ionization of bulk H_2 by cosmic rays. Thus the omission of cosmic rays cuts off the dominant mechanism by which gas-phase NH_3 is created. Similarly, the gaseous reservoir of water is largely maintained by the UV photodesorption of solid-phase water. Thus, a decrease in the flux of ultraviolet radiation leads to a decrease in the abundance of gas-phase water.
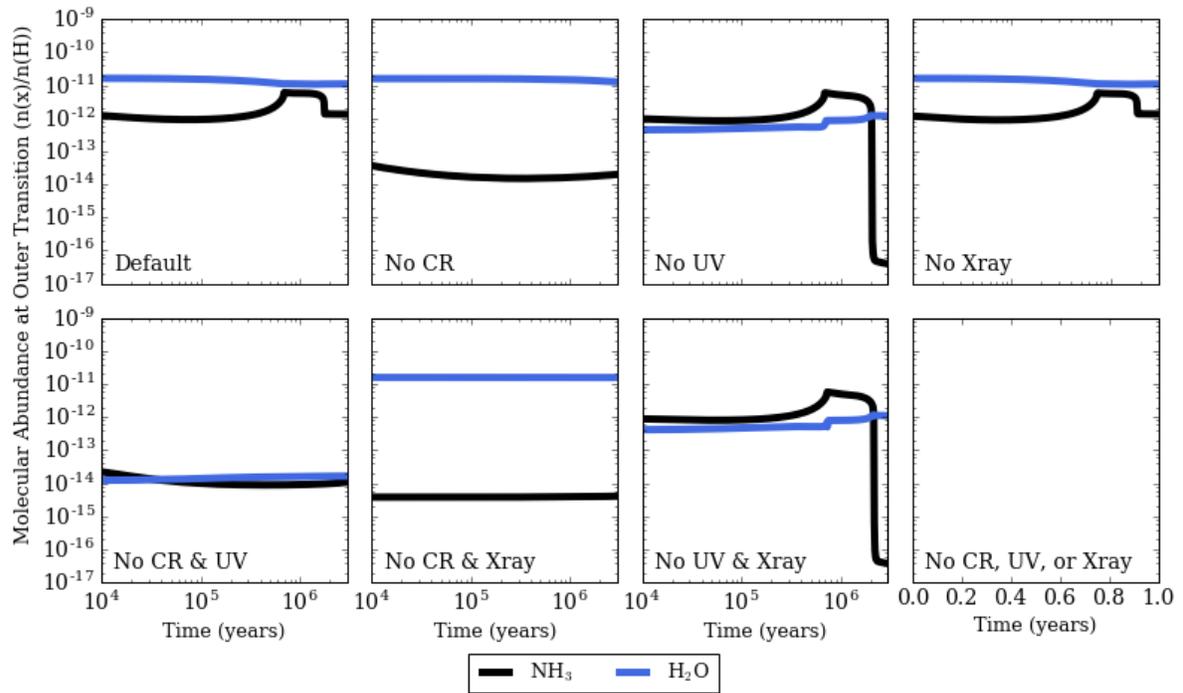
Figure 5.2: Evolution of gas-phase ammonia (black) and water (blue) abundances over the chemical lifetime of the disk model for various combinations of ionizing radiation sources as in Figure 5.1. Shown is the outer (R = 55 AU) transition region (Z = 10 AU), where the fiducial model returns a high gas-phase ammonia-to-water ratio.

46

Chapter 6:
Effects of Inherited Ammonia

The previous chapters have included tests that were conducted with low initial amounts of ammonia: 8×10^{-8} n(NH$_3$)/n(H) (as specified in Aikawa & Herbst (1999) Fig. 5a). By modeling systems with a negligible amount of ammonia present at the onset of disk development, we were able to observe how ammonia is produced and destroyed by the conditions within the disk itself.

However, observations of protostars by Öberg et al. (2011) suggest that the actual ammonia-to-water ratio is 5% and the ammonia abundance inherited by circumstellar disks is closer to 1.25×10^{-5} n(NH$_3$)/n(H). To determine if the chemical characteristics of the system are affected by adopting this substantial initial ammonia abundance, the code was run again under fiducial physical conditions (as shown in Tables 2.2 and 3.1) but with the initial ammonia abundance at 5% NH$_3$/H$_2$O, or 1.25×10^{-5} n(NH$_3$)/n(H), as compared to the fiducial value of 8×10^{-8}.
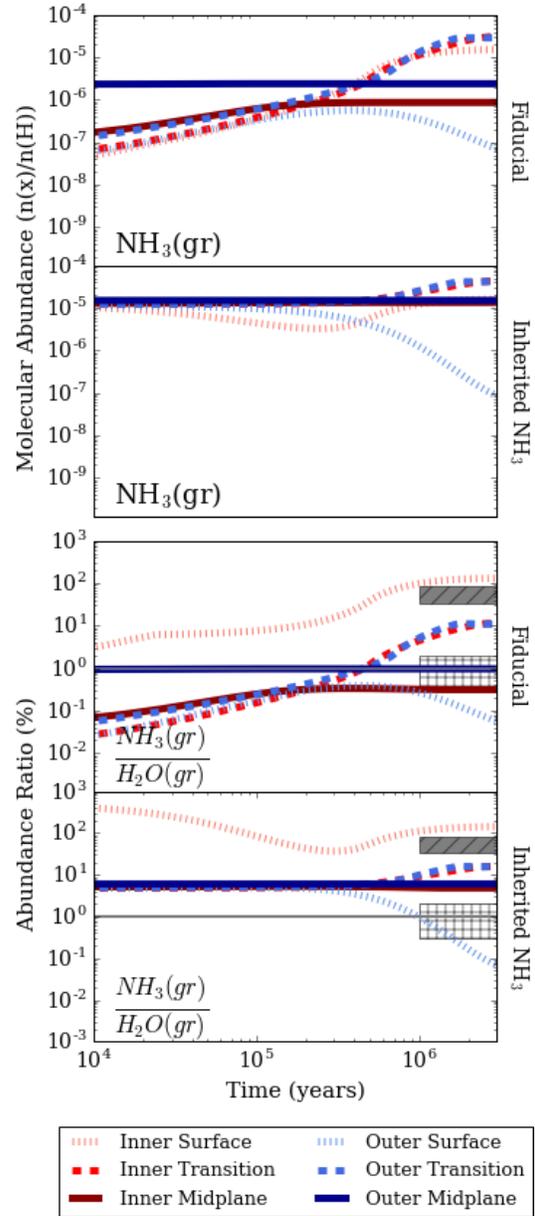
Figure 6.1: Same as Figures 3.1 and 4.1, showing only ammonia ice abundances and ratios, with the second and fourth rows representing the case with high abundances of inherited ammonia. Diagonal hatching represents the Salinas et al. (2016) gas-phase result; crossed hatching represents the Mumma & Charnley (2011) cometary result.

Our models show that the gas phase ammonia abundances at 3 Myrs are unaffected by the increased inheritance of 5% ammonia to water. This result suggests that inherited ammonia is reprocessed by gas-phase disk chemistry. Despite increasing the global initial ammonia by a factor of 150, the gas-phase ammonia chemistry at 3 Myr remained almost completely unchanged. However, ammonia ice increases by $\lesssim 2$ orders of magnitude when inheritance is included, as shown in shown in Figure 6.2.

The chemical effects of ionization were also examined in the case of elevated initial ammonia; the code was re-run with various permutations of radiation sources removed as in §5. In most cases the same trend is repeated: the gas-phase ratio is not affected by inherited ammonia, while the ice-phase ratio is greatly affected. However, it is important to note that in the No CR case, the gas-phase ratio in the outer transition region increased from ~0.1% in the low-inheritance case to ~10% in the high-inheritance case: bringing the No CR ratio to within a factor of 3 of the Salinas et al. (2016) range.

Ice-phase NH_3/H_2O ratios for each ionization environment are shown in Figure 6.3. While ice variations between the fiducial ionization rates and the depleted ionization rates remain small, differing by at most a factor of 2, the variations between the low-inheritance and high-inheritance case are drastic. In every case, the inherited ammonia model leads to a ratio that is 1–2 orders of magnitude greater than the fiducial model. While
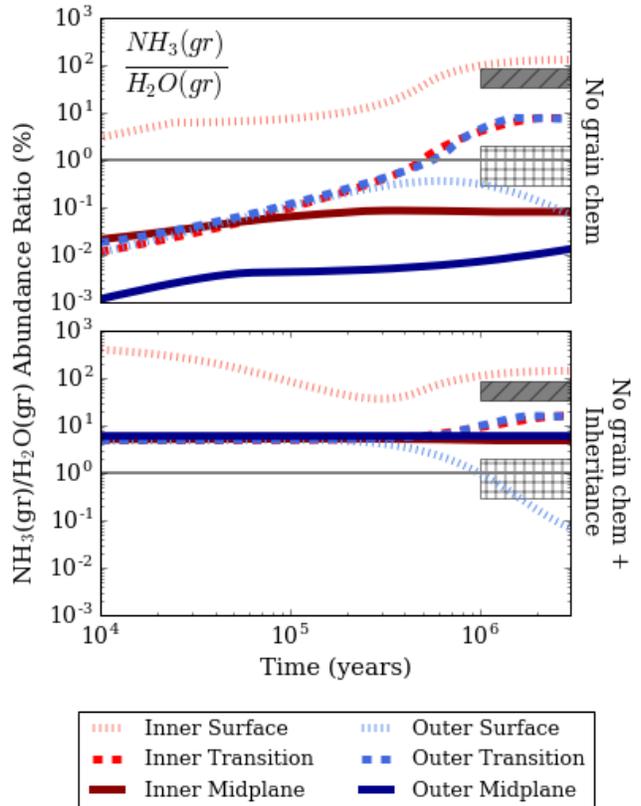
Figure 6.2: Same as Figures 3.1 and 4.1, showing only ammonia ice ratios. The first row represents the case without ammonia formation on grains, and the second row represents the 5% inheritance case without ammonia formation on grains. Dark diagonal hatching represents the Salinas et al. (2016) gas-phase result; light crossed hatching represents the Mumma & Charnley (2011) cometary result.

48

ice-phase ratios in the fiducial model are all at or just below the Mumma & Charnley (2011) range of cometary NH_3/H_2O ratios, all models with inheritance are above cometary values.
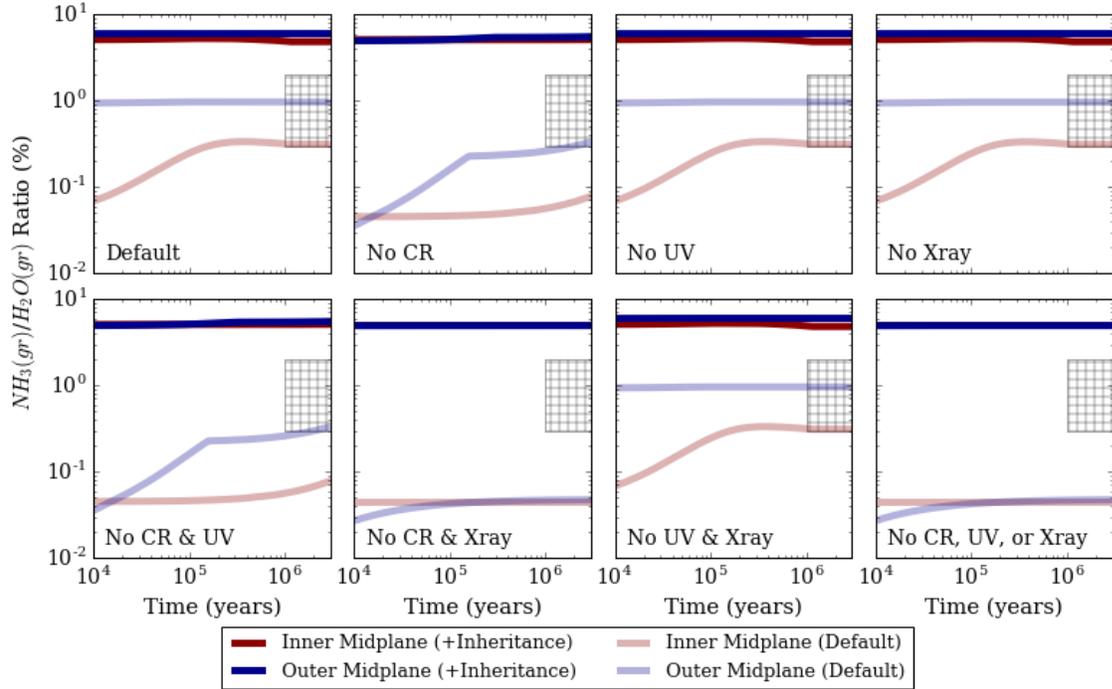
Figure 6.3: Evolution of ice-phase ammonia-to-water ratios in the inner and outer midplane over the chemical lifetime of the disk model for various combinations of ionizing radiation sources (X-rays, cosmic rays, and ultraviolet rays). Dark lines represent the case with 5% inherited ammonia, while faded lines represent the case without inheritance (as first shown in Figure 5.1). The hatched regions represent the cometary abundance ratio range (0.3–2%), as reported in Mumma & Charnley (2011).

Chapter 7:
Discussion

The calculations presented in this thesis explore the sensitivity of gas- and grain-phase ammonia chemistry in disks to both physical and chemical factors. We consider the importance of the physical disk environment, including spatial location within the disk and the effects of ionizing radiation. We trace the chemical pathways of ammonia formation both in the gas-phase and ice-phase, and identify key reactions and reactants. Finally, we evaluate the footprint of initial chemical conditions in varying disk environments. When considered together, it becomes clear that these physical and chemical processes interact with each other constructively and destructively, altering the characteristics of ammonia reservoirs and the corresponding ammonia-to-water ratios.

7.1   Importance of Location

In Chapter 3, we demonstrate that the active ammonia formation and destruction pathways change with position in the disk. We consider six different test locations that span inner and outer regions of the disk and three vertical locations from the disk surface to the midplane. Across these six regions, the gas-phase ammonia-to-water ratios range from $< 10^{-7}$ in the midplane to ~1 in upper disk regions. The range in the ice-phase ratios is smaller, yet still spans three orders of magnitude from ~0.001 in the outer midplane to ~1 at the inner surface. The ice-phase and gas-phase ratios in a single location do not always correlate.

These spatial variations can be explained by three elements: (1) differing degrees and types of ionizing radiation, (2) differences between grain-phase and ice-phase chemistry and (3) difference between NH_3 chemistry and H_2O chemistry.

Gas-phase ammonia, like water vapor, exists in greater abundances in regions of the

disk where photodesorption occurs at a higher rate. Thus, gas-phase abundance generally increases with vertical distance from the midplane and decreases with radial distance from the star. By the same reasoning, ice-phase ammonia exists in lesser abundances in more heavily-radiated regions of the disk, and ice-phase abundance both decreases with vertical distance from the midplane and increases with radial distance from the star. Thus, regional changes in radiative flux can explain changes in the ammonia abundances.

Additionally, the formation processes for gas-phase versus ice-phase ammonia differ (see §7.2). At a given location, the ice-phase and gas-phase ratios are not necessarily correlated. This is especially true in the ice-dominated midplane, where gas-phase ammonia-to-water ratios plummet to fractions of a percent while ice-phase ratios remain close to 1%. These results suggest that more is occurring chemically than just adsorption and desorption; active gas-phase chemistry alters both ammonia and water chemistry such that the gas ratios do not always follow the ice ratios.

Relatedly, changes in the NH_3/H_2O ratios clearly incorporate another component: water. Collings et al. (2004) and Öberg (2009) found that ammonia and water are adsorbed and desorbed at similar rates and by similar mechanisms, and Salinas et al. (2016) assumes that they are co-spatial in TW Hydra. Thus if the gas-phase NH_3 and H_2O abundances in disks were determined by adsorption and desorption alone, the absolute ammonia abundances and absolute water abundances would mirror one another, differing only by a constant multiplicative factor. This is not the case. Our work shows that gas-phase ammonia and water abundances evolve distinctly due to dissimilar gas-phase processing between the two species, leading to strong regional differences in the two ratios. This result problematizes the common assumption of co-spatial ammonia and water in disks.

7.2 Ionization and Ammonia Formation

Our results clearly indicate the importance of different ionizing radiation sources in determining how much ammonia exists at different places and times within the disk. Ions play a significant role as the initial abundances of N and N_2 present in the stellar birth cloud evolve into NH_3 and $NH_3(gr)$. By tracing reactions involving ammonia using the methods described in §2.4 and mapping out ammonia production and destruction pathways, for both gas and ice, we shed light on the specific ions and chemical processes that are most crucial for ammonia chemistry. Such maps of ammonia production and destruction are presented in Figures 7.1 and 7.2.

As shown in Figure 7.1, gas-phase ammonia is produced by a chain of hydrogenation reactions in which more and more hydrogen atoms are bonded to existing ionized nitrogen or ionized nitrogen hydrides. There are two possible points of entrance into the hydrogenation chain, the secondary being at the trivial N^+, but the primary being at NH_2^+.

N^+ is created by interactions of nitrogen-bearing molecules such as NH, HCN, N_2, NH_2, NO, CN, etc. with ionized Helium, He^+. Helium is ionized by cosmic rays and X-rays. While N^+ can also be created directly by the cosmic ray ionization of N, this reaction is much more infrequent – Helium is over 6,000 times more abundant in the disk than N.

NH_2^+, by comparison, is created by a much more favorable series of reactions:

$$N_2 + H_3^+ \rightarrow N_2H^+ + H_2 \tag{7.1}$$

$$N_2H^+ + e^- \rightarrow NH + N^+ \tag{7.2}$$

$$NH + ion \rightarrow NH_2^+ + ? \tag{7.3}$$
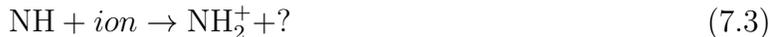
Indeed, analysis of model results shows that N_2 is present in the disk at high levels (inherited at 9% N_2/H_2O), and H_3^+ is created primarily by reactions of H_2^+ with the bulk gas reservoir
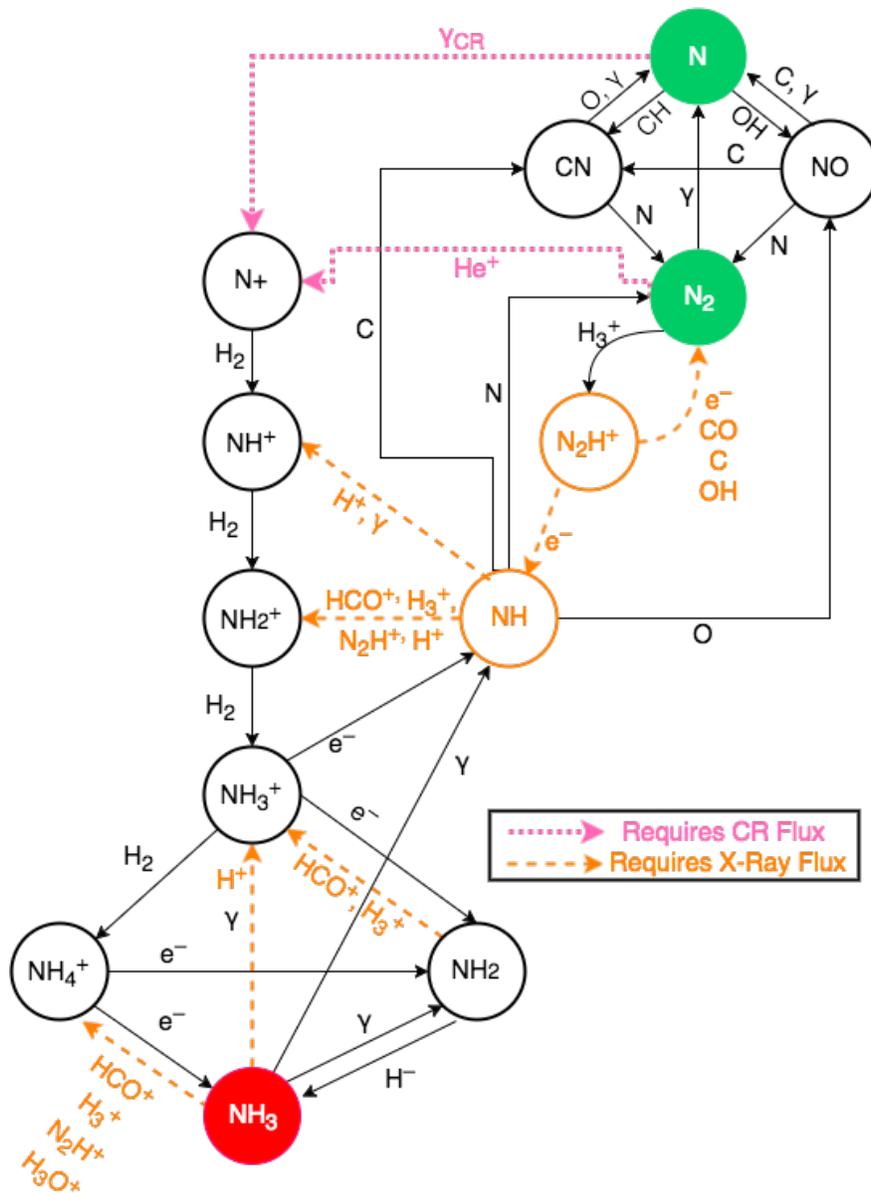
Figure 7.1: Pathways of production and destruction of gas-phase ammonia, shown in red, beginning with atomic and molecular nitrogen (N and N_2), shown in green. Each arrow represents a chemical reaction moving from a reactant to a product. Arrows colored pink and orange are strongly affected by the presence of cosmic rays or X-rays, respectively. UV photons are represented by *gamma*, while cosmic rays are represented by γ_{CR}.

of H_2. H_2^+, in turn, is created by the ionization of H_2 by cosmic rays. (While H_2 can also be ionized by X-ray or UV photons, these ionizations occur at orders of magnitude lower rates.) As there is 3.5 times more H_2 than He in a disk with a typical galactic cosmic ray flux, H_3^+ is much more abundant than He^+, and thus ammonia is formed most efficiently via the $N_2 \rightarrow N_2H^+$ pathway.

Ammonia is destroyed by interactions with ions such as H_3^+, HCO^+, N_2H^+, H^+, and H_3O^+. These ions are all created primarily by cosmic ray ionization. At the disk surface, ammonia is also destroyed by UV photons at a rate comparable that of dissociative recombination with ions.

Ice-phase ammonia is produced in a different chain: hydrogenation reactions that occur on the grain surface itself, bonding frozen H(gr) atoms to existing N(gr) or NH_X(gr) molecules (Fig. 7.2). Here there are as many points of entrance as there are steps in the chain: any gaseous nitrogen hydride can adsorb onto the surface of the grain and become ice (and vice versa). The importance of ionization in the production
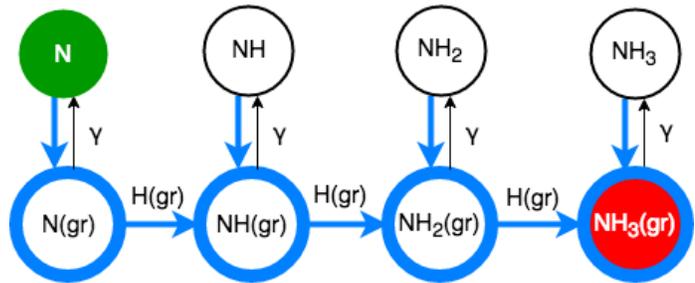
Figure 7.2: Pathways of production and destruction of ice-phase ammonia, shown in red, beginning with atomic nitrogen (N), shown in green. Each arrow represents a chemical reaction moving from a reactant to a product. Blue arrows and circles represent molecules and reactions that occur as ices on dust grains. Desorption, denoted by γ, can occur as thermal desorption or photodesorption by UV photons or cosmic rays.

of gas phase ammonia manifests in (1) the role of ions in gas-phase production of NH, NH_2, and NH_3, as previously described, and (2) the photodesorption of grain-phase molecules by cosmic rays and UV photons, if present. Grain-phase chemistry is necessary to achieve cometary abundances of ammonia ice in the absence of inheritance. As shown in Figure 4.1, when ammonia is not formed on grains, the NH_3(gr)/H_2O(gr) ratio in the comet-forming midplane does not reach 0.3%, the lower bound of the cometary ice abundance as determined from comets (Mumma & Charnley, 2011).

Thus, throughout the disk, cosmic rays are an integral part of ammonia production. Cosmic rays kick-start the gas-phase ammonia production chain by ionizing inherited reservoirs of nitrogen and hydrogen. In their absence, the primary pathways by which ammonia is created are cut off, leading to a decrease in ammonia abundance of ~3 orders of magnitude in the gas-phase and a factor of 3 in the ice-phase.

7.3 Chemical Inheritance

We show that the initial ammonia chemistry present in the disk has significant effects on ammonia chemistry in the midplane and ice chemistry throughout the disk. Yet, while chemical processes such as grain-surface chemistry and inherited chemistry are integral to the chemical evolution of protoplanetary disks, their effects are less noticeable in the upper disk regions. Ammonia gas chemistry in the transition and surface regions is largely unaffected by chemical inheritance, as chemistry in these heavily-radiated regions is driven and essentially 'reset' by ionizing radiation that destroys and reconfigures existing chemistry. It is the midplane where chemical inheritance, via ice chemistry, plays a major role.

When considered alongside the effects of various ionization sources, the importance of ammonia inheritance becomes more apparent. There is increasing evidence that disks may experience depleted cosmic ray flux; Cleeves et al. (2013a) suggest that the strong presence of stellar winds around young stars serves to deflect galactic cosmic rays, ultimately leading to cosmic ray ionization rates 10–1000 times lower than in the ISM. Such results suggest that disk models without cosmic rays may in fact be the most realistic disk environments. In the model without substantial ammonia inheritance, the removal of cosmic rays reduced the ice-phase ammonia-to-water ratio to sub-cometary levels; as shown in Figure 5.1, $NH_3(gr)/H_2O(gr)$ in the midplane peaks around 0.1% at 3 Myr. Grain surface chemistry alone is not sufficient to reach cometary ice ratios in the absence of cosmic rays. However, in the case of 5% NH_3/H_2O inheritance, the inherited ammonia becomes trapped in the

ice reservoir and the $NH_3(gr)/H_2O(gr)$ ratio rises to almost 5% – reaching and surpassing cometary abundance. We thus conclude that, in the absence of cosmic rays, ammonia must be inherited to reach observed ice abundances.

Chemical inheritance also renders ice-phase formation of ammonia unnecessary. In models where 5% NH_3/H_2O inheritance is included and the formation of ammonia on grains is excluded, midplane ice abundances surpass the 0.3–2% range.

It is worthwhile to note that this conclusion and methodology in many ways mirrors and draws upon that of Cleeves et al. (2014b), who compared low- and high-inheritance models to assert that the fraction of deuterated water on Earth is too high to have been created solely from chemical evolution during our Solar System's disk era; some proportion of pristine deuterated water must have been inherited from the Sun's birth cloud (the ISM). Similarly, we find that the observed abundance of gas-phase ammonia in disks is too high to have been created solely from internal chemical processing of fundamental molecules such as N, N_2, and H_2 during disk evolution; a significant proportion of ammonia must have been inherited from the ISM.

7.4   Comparison with Observations

The Mumma & Charnley (2011) result has been recreated by our model under multiple conditions. In a disk that does not inherit significant interstellar ammonia, cometary levels of ammonia ice can be produced in the presence of high cosmic ray flux. In the absence of cosmic rays, however, such a disk does not reach cometary ammonia ice abundances. Similarly, in a disk without ammonia inheritance, grain-surface formation of ammonia is necessary to reach the 0.3–2% $NH_3(gr)/H_2O(gr)$ cometary range; if grain-surface formation is omitted, cometary abundances cannot be reached. However, in the case of 5% ammonia inheritance with respect to water, the Mumma & Charnley (2011) cometary ice abundance is achievable in all cases, regardless of ionizing radiation or grain-surface chemistry. Thus,

we emphasize the importance of interstellar chemistry for the evolution of ice chemistry in disks.

Our results also quell the controversy introduced by the high gas-phase NH_3/H_2O ratio found by Salinas et al. (2016). We find that our models recreate these high (~10–100%) ratios, but only in the upper regions of the disk. Furthermore, model ice ratios, even in the case of inheritance, do not reach even the very lowest end of the 33–84% range, suggesting that the Salinas et al. (2016) *Herschel* observation is not probing the ice reservoir, but rather the ammonia gas reservoir in upper disk regions.

While cosmic rays play a large role gas-phase ammonia production, even in their absence Salinas et al. (2016) levels of ammonia gas can be produced by X-ray ionization in the inner disk surface. Due to chemical gas-phase reprocessing in these heavily radiated disk regions, our results show similar trends in both the presence and absence of ammonia inheritance and grain-surface ammonia formation.

Chapter 8:
Conclusion and Future Directions

The fiducial box model results as shown in Figure 3.1 reveals that a single disk can simultaneously support the elevated gas-phase NH_3/H_2O ratio reported by Salinas et al. (2016) and the lower ice-phase ratio as extrapolated from comet data. While the ratio and molecular abundances vary spatially across the disk, the gas-phase ratio exceeds 10% at the inner surface and in both the inner and outer transition regions – the regions which the observations of Salinas et al. (2016) likely probe. An elevated ammonia-to-water ratio in only certain disk locations could lead to an elevated total measured ratio in an unresolved observation of the disk, such as the observation of TW Hydra with *Herschel* by Salinas et al. (2016). Furthermore, the model returned a grain-phase $NH_3(gr)/H_2O(gr)$ ratio that agrees with the measured ice-phase ammonia-to-water ratio of 0.3–2% as measured in over ten comet observations (Mumma & Charnley, 2011). To summarize, our results suggest that:

1. A high gas-phase NH_3/H_2O ratio as observed by Salinas et al. (2016) can exist at the disk surface, simultaneously with a low ice-phase NH_3/H_2O as observed by Mumma & Charnley (2011) in the disk midplane.

2. Regional differences in ammonia and water chemistry occur due to varying rates of ionization throughout the disk, with a strong dependence on cosmic rays.

3. In the case of modulated cosmic ray flux, as suggested by Cleeves et al. (2015), it becomes necessary to include inherited ammonia to reach observed cometary abundances of ammonia ice.

However, many questions remain to be pursued. Le Gal et al. (2014) suggests that nitrogen hydride chemistry depends on chemical inheritance not just of nitrogen and nitrogen hydrides, but also of sulfur, carbon, and oxygen. In addition, many time-dependent processes

occur in disks which our model does not treat, including radial drift, grain growth, vertical grain settling, turbulence, stellar winds, and grain collisions; a more complete model will take such processes into account. In future work, we will incorporate the answers to these qualitative questions and others into quantitative global models in an attempt to create synthetic observations to compare to the Salinas et al. 2016 detection and verify our new theories. This work also motivates further observations of ammonia and related molecules with the newest observatories, such as observations of NH_2D with ALMA.

Numerical astrochemical modeling serves as a powerful tool allowing astrochemists to explore the chemical intricacies of distant systems. Especially in the era of ALMA, such a tool enables theoretical investigations that complement and enhance our understanding of even the highest-resolution spectral observations. As the field of astrochemistry advances, it is becoming increasingly evident that the complex chemistry of Earth and the Solar System is not the exception, but rather the rule (Öberg et al., 2015). Yet in addition to the push to study ever-more-complex chemistry outside of our Solar System, there must be a simultaneous push to revisit chemical foundations and to obtain a deeper understanding of the myriad processes that determine the chemical evolution of even 'simple' molecules such as NH_3.

Chapter 9:
Acknowledgements

I am deeply thankful for the guidance, support, and patience that my mentors Hector Arce, Karin Öberg, and Ilse Cleeves have provided me over the past nine months. The rigor of the project is a result of their ceaseless encouragement for me to keep exploring and deepening my understanding of every facet of this work. I am also grateful for the kind and welcoming faculty in the Yale astronomy and physics departments who have advised me over my four years here, namely Louise Edwards, Sarbani Basu, Debra Fischer, Sarah Demers, Meg Urry, Marla Geha, and Priyamvada Natarajan. I want to extend special thanks to Reina Maruyama, for advising my junior year research project in particle astrophysics, and continuing to mentor and support me ever since. Words are inadequate to express my gratitude for the leaders of the 2016 Banneker and Aztlán Institutes, John Johnson and Jorge Moreno, who work endlessly to educate and support aspiring astronomers of color such as myself. Thank you also to the upcoming classes of astronomy majors, who continually inspire me with their devotion, curiosity, and remarkable compassion for one another. Finally, thank you to my family and close friends for your unwavering belief in my ability to succeed in physics. As I move forward with my career in the coming years, I know I will always look back and cherish the time I have spent learning and growing within the Yale astronomy community.

Bibliography

Aikawa, Y. & Herbst, E. 1999, A&A, 351, 233

Aikawa, Y., Miyama, S. M., Nakano, T., & Umebayashi, T. 1996, ApJ, 467, 684

Aikawa, Y., van Zadelhoff, G. J., van Dishoeck, E. F., & Herbst, E. 2002, A&A, 386, 622

Andre, P., Ward-Thompson, D., & Barsony, M. 1993, ApJ, 406, 122

Andrews, S. M. & Williams, J. P. 2005, ApJ, 631, 1134

Andrews, S. M., Wilner, D. J., Hughes, A. M., Qi, C., & Dullemond, C. P. 2010, The Astrophysical Journal, 723, 1241

Andrews, S. M., Wilner, D. J., Hughes, A. M., Qi, C., Rosenfeld, K. A., Öberg, K. I., Birnstiel, T., Espaillat, C., Cieza, L. A., Williams, J. P., Lin, S.-Y., & Ho, P. T. P. 2012, ApJ, 744, 162

Andrews, S. M., Wilner, D. J., Zhu, Z., Birnstiel, T., Carpenter, J. M., Pérez, L. M., Bai, X.-N., Öberg, K. I., Hughes, A. M., Isella, A., & Ricci, L. 2016, ApJL, 820, L40

Bergin, E., Calvet, N., D'Alessio, P., & Herczeg, G. J. 2003, ApJL, 591, L159

Bergin, E. A. 2009, ArXiv e-prints

Bergin, E. A., Cleeves, L. I., Crockett, N. R., Favre, C., & Neill, J. L. 2013, in Astronomical Society of the Pacific Conference Series, Vol. 476, New Trends in Radio Astronomy in the ALMA Era: The 30th Anniversary of Nobeyama Radio Observatory, ed. R. Kawabe, N. Kuno, & S. Yamamoto, 185

Bernstein, M. P., Dworkin, J. P., Sandford, S. A., Cooper, G. W., & Allamandola, L. J. 2002, Nature, 416, 401

Bottinelli, S., Boogert, A. C. A., Bouwman, J., Beckwith, M., van Dishoeck, E. F., Öberg, K. I., Pontoppidan, K. M., Linnartz, H., Blake, G. A., Evans, II, N. J., & Lahuis, F. 2010, ApJ, 718, 1100

Bringa, E. M. & Johnson, R. E. 2004, ApJ, 603, 159

Charnley, S. B., Rodgers, S. D., & Ehrenfreund, P. 2001, A&A, 378, 1024

Cheung, A. C., Rank, D. M., Townes, C. H., Thornton, D. D., & Welch, W. J. 1968, Physical Review Letters, 21, 1701

Cleeves, L. I. 2015, PhD thesis, University of Michigan

Cleeves, L. I., Adams, F. C., & Bergin, E. A. 2013a, ApJ, 772, 5

Cleeves, L. I., Adams, F. C., Bergin, E. A., & Visser, R. 2013b, ApJ, 777, 28

Cleeves, L. I., Bergin, E. A., & Adams, F. C. 2014a, ApJ, 794, 123

Cleeves, L. I., Bergin, E. A., Alexander, C. M. O'D., Du, F., Graninger, D., Öberg, K. I., & Harries, T. J. 2014b, Science, 345, 1590

Cleeves, L. I., Bergin, E. A., Qi, C., Adams, F. C., & Öberg, K. I. 2015, ApJ, 799, 204

Collings, M. P., Anderson, M. A., Chen, R., Dever, J. W., Viti, S., Williams, D. A., & McCoustra, M. R. S. 2004, MNRAS, 354, 1133

D'Alessio, P., Calvet, N., Hartmann, L., Lizano, S., & Cantó, J. 1999, ApJ, 527, 893

Dame, T. M., Hartmann, D., & Thaddeus, P. 2001, ApJ, 547, 792

Draine, B. T. 2003, ARA&A, 41, 241

—. 2006, ApJ, 636, 1114

Durisen, R. H. Disk Hydrodynamics, ed. P. J. V. Garcia (University of Chicago Press), 149–236

Faure, A., Hily-Blant, P., Le Gal, R., Rist, C., & Pineau des Forêts, G. 2013, ApJL, 770, L2

Fedoseev, G., Ioppolo, S., Zhao, D., Lamberts, T., & Linnartz, H. 2015, MNRAS, 446, 439

Fogel, J. K. J., Bethell, T. J., Bergin, E. A., Calvet, N., & Semenov, D. 2011, ApJ, 726, 29

Furlan, E., Hartmann, L., Calvet, N., D'Alessio, P., Franco-Hernández, R., Forrest, W. J., Watson, D. M., Uchida, K. I., Sargent, B., Green, J. D., Keller, L. D., & Herter, T. L. 2006, ApJS, 165, 568

Hartmann, L. 1998, Cambridge Astrophysics Series, Vol. 32, Accretion Processes in Star Formation, 2nd edn. (Cambridge, UK: Cambridge University Press)

Hasegawa, T. I. & Herbst, E. 1993, MNRAS, 261, 83

Hasegawa, T. I., Herbst, E., & Leung, C. M. 1992, ApJS, 82, 167

Hiraoka, K., Yamashita, A., Yachi, Y., Aruga, K., Sato, T., & Muto, H. 1995, ApJ, 443, 363

Igea, J. & Glassgold, A. E. 1999, ApJ, 518, 848

Isella, A. 2006, PhD thesis, Universita' degli Studi di Milano

Isella, A., Carpenter, J. M., & Sargent, A. I. 2009, ApJ, 701, 260

Lada, C. J. 1987, in IAU Symposium, Vol. 115, Star Forming Regions, ed. M. Peimbert & J. Jugaku, 1–17

Lada, C. J. & Wilking, B. A. 1984, ApJ, 287, 610

Le Gal, R., Hily-Blant, P., Faure, A., Pineau des Forêts, G., Rist, C., & Maret, S. 2014, A&A, 562, A83

Lee, H.-H., Herbst, E., Pineau des Forets, G., Roueff, E., & Le Bourlot, J. 1996, A&A, 311, 690

Lynden-Bell, D. & Pringle, J. E. 1974, MNRAS, 168, 603

Mandell, A. M., Bast, J., van Dishoeck, E. F., Blake, G. A., Salyk, C., Mumma, M. J., & Villanueva, G. 2012, ApJ, 747, 92

Mathis, J. S., Rumpl, W., & Nordsieck, K. H. 1977, ApJ, 217, 425

McCaughrean, M. J. & O'dell, C. R. 1996, AJ, 111, 1977

Megeath, S. T., Gutermuth, R., Muzerolle, J., Kryukova, E., Flaherty, K., Hora, J. L., Allen, L. E., Hartmann, L., Myers, P. C., Pipher, J. L., Stauffer, J., Young, E. T., & Fazio, G. G. 2012, AJ, 144, 192

Mumma, M. J. & Charnley, S. B. 2011, ARA&A, 49, 471

Öberg, K. I. 2009, PhD thesis, Leiden University

Öberg, K. I., Boogert, A. C. A., Pontoppidan, K. M., van den Broek, S., van Dishoeck, E. F., Bottinelli, S., Blake, G. A., & Evans, II, N. J. 2011, ApJ, 740, 109

Öberg, K. I., Guzmán, V. V., Furuya, K., Qi, C., Aikawa, Y., Andrews, S. M., Loomis, R., & Wilner, D. J. 2015, Nature, 520, 198

Salinas, V. N., Hogerheijde, M. R., Bergin, E. A., Cleeves, L. I., Brinch, C., Blake, G. A., Lis, D. C., Melnick, G. J., Panić, O., Pearson, J. C., Kristensen, L., Yıldız, U. A., & van Dishoeck, E. F. 2016, A&A, 591, A122

Sargent, A. I. & Beckwith, S. 1987, ApJ, 323, 294

Schwarz, K. R. & Bergin, E. A. 2014, ApJ, 797, 113

Semenov, D., Hersant, F., Wakelam, V., Dutrey, A., Chapillon, E., Guilloteau, S., Henning, T., Launhardt, R., Piétu, V., & Schreyer, K. 2010, A&A, 522, A42

Shu, F. H., Adams, F. C., & Lizano, S. 1987, ARA&A, 25, 23

Smith, I. W. M., Herbst, E., & Chang, Q. 2004, MNRAS, 350, 323

Smith, N., Bally, J., Licht, D., & Walawender, J. 2005, AJ, 129, 382

Stahler, S. W. 1988, ApJ, 332, 804

Tielens, A. G. G. M. & Hagen, W. 1982, A&A, 114, 245

van Dishoeck, E. F. 2006, Proceedings of the National Academy of Science, 103, 12249

Visser, R., van Dishoeck, E. F., Doty, S. D., & Dullemond, C. P. 2009, A&A, 495, 881

Weidenschilling, S. J. 1977, Ap&SS, 51, 153

Williams, J. P. & Cieza, L. A. 2011, ARA&A, 49, 67

Woodall, J., Agúndez, M., Markwick-Kemper, A. J., & Millar, T. J. 2007, A&A, 466, 1197